



# Model evaluation experiments in the North Atlantic Basin: simulations in nonlinear terrain-following coordinates

Dale B. Haidvogel <sup>a,\*</sup>, Hernan G. Arango <sup>a</sup>, Kate Hedstrom <sup>a</sup>,  
Aike Beckmann <sup>b</sup>, Paola Malanotte-Rizzoli <sup>c</sup>,  
Alexander F. Shchepetkin <sup>d</sup>

<sup>a</sup> Institute of Marine and Coastal Sciences, Rutgers University, New Brunswick, NJ, USA

<sup>b</sup> Alfred-Wegener-Institute for Polar and Marine Research, Bremerhaven, Germany

<sup>c</sup> Department of Earth, Atmospheric and Planetary Sciences, Massachusetts Institute of Technology, Cambridge, MA, USA

<sup>d</sup> Institute of Geophysics and Planetary Physics, University of California at Los Angeles, Los Angeles, CA, USA

Received 26 August 1998; received in revised form 4 August 1999; accepted 3 February 2000

---

## Abstract

A primitive equation ocean circulation model in nonlinear terrain-following coordinates is applied to a decadal-length simulation of the circulation in the North Atlantic Ocean. In addition to the stretched sigma coordinate, novel features of the model include the utilization of a weakly dissipative, third-order scheme for tracer advection, and a conservative and constancy-preserving time-stepping algorithm. The objectives of the study are to assess the quality of the new terrain-following model in the limit of realistic basin-scale simulations, and to compare the results obtained with it against those of other North Atlantic models used in recent multi-model comparison studies.

The new model is able to reproduce many features of both the wind-driven and thermohaline circulation, and to do so within error bounds comparable with prior model simulations (e.g., CME and DYNAMO). Quantitative comparison with comparable results obtained with the Miami Isopycnic Coordinate Model (MICOM) show our terrain-following solutions are of similar overall quality when viewed against known measures of merit including meridional overturning and heat flux, Florida Straits and Gulf Stream transport, seasonal cycling of temperature and salinity, and

---

\* Corresponding author. Tel.: +1-732-932-6555, ext. 256; fax: +1-510-643-1142.

E-mail address: dale@ahab.rutgers.edu (D.B. Haidvogel).

upper ocean currents and tracer fields in the eastern North Atlantic Basin. Sensitivity studies confirm that the nonlinear vertical coordinate contributes significantly to model fidelity, and that the global inventories and spatial structure of the tracer fields are affected in important ways by the choice of lateral advection scheme. © 2000 Elsevier Science B.V. All rights reserved.

**Keywords:** North Atlantic Basin; Nonlinear terrain-following coordinates; Ocean circulation

---

## 1. Introduction

The North Atlantic is by far the most intensely studied of the World's oceans. Although primarily a result of geographical accessibility and importance, and its relatively modest size, interest in the North Atlantic Basin (NAB) has also been prompted by its unique dynamical characteristics — e.g., the strongest western boundary current, multiple interbasin exchanges, formation of deep water masses, and other properties. Over the past three decades, a variety of intensive local and basin-scale observational programs — including MODE/POLYMODE, SYNOP, TOPOGULF, TOURBILLON, SEQUAL, WESTRAX and most recently WOCE — have led to a detailed description of its hydrography and circulation. Many theoretical concepts of broad significance to physical oceanography (e.g., westward intensification and the ventilated thermocline) have been developed in part to account for its observed properties.

Despite this rich theoretical and observational framework, many fundamental processes in the NAB are either not fully understood or not directly observable, and have therefore been the focus of numerical simulation. Among these are the separation of the Gulf Stream, the strength and structure of the meridional transports of mass and heat, mode water formation and subduction, the patterns and nonlinear dynamics of mesoscale eddies, and interbasin exchange with the Mediterranean and Nordic Seas. For several reasons, however, direct simulation of the wind-driven and thermohaline circulation of the North Atlantic has thus far been inconclusive. A principal source of uncertainty has been the sensitivity of numerical results to model-related choices such as horizontal and vertical resolution, vertical coordinate system, and subgrid-scale closure. Since simulations with “infinite” spatial resolution are impossible, there is no numerically “exact” answer with which to compare, and progress can only be made by systematic study of model sensitivities on the one hand, and by quantitative comparison against the accumulating observational database on the other.

In response to the need for systematic model studies, the Community Modeling Effort (CME) was initiated in the mid-1980s at the National Center for Atmospheric Research (NCAR). The CME configuration (Bryan and Holland, 1989), based on the Geophysical Fluid Dynamics Laboratory (GFDL)  $z$ -coordinate ocean circulation model (e.g., Bryan, 1969; Cox, 1984) at  $1/3 \times 1/5^\circ$  resolution, became a standard for basin-wide applications of ocean circulation models. Driven by monthly mean surface climatologies and bounded by buffer zones in the north and south and in the Gulf of Cadiz, the influence of forcing functions, subgrid-scale parameterizations, and resolution was evaluated (Böning and Bryan, 1996).

By the early 1990s, the influence of alternate vertical coordinate systems became a central issue in basin-scale modeling. A number of two-way intercomparisons were initially conducted (Chassignet et al., 1996; Roberts et al., 1996; Marsh et al., 1996), leading to a systematic attempt to evaluate the performance of different oceanic general circulation models in the DYNAMO project [jointly carried out by researchers from three European institutions using the MOM (Pacanowski, 1996), MICOM (Bleck et al., 1992) and SPEM (Haidvogel et al., 1991) ocean models].

The DYNAMO configuration differed from the CME in three aspects: the domain extends to 70°N (including the Greenland–Iceland–Scotland Ridge system and the important overflow regions); it uses an isotropic grid (thus adding resolution at higher latitudes); and it uses a consistent set of surface forcing fields [a 3-year climatology from the ECMWF (Barnier et al., 1995)]. All three DYNAMO models use identical horizontal grids and share as many other parameters as possible. For further details on the model configuration and a complete account of the results, see the report by the DYNAMO Group (1997; hereafter, DG97).

Although the configuration of the three DYNAMO models is closer than for previous model–model comparisons, it is still difficult to attribute model differences unequivocally to the vertical coordinate system, especially since the different vertical coordinate systems used yield differences in bathymetry and near-bottom resolution. Three areas, however, can be identified wherein we can safely assume that the vertical coordinate is the main contributing factor. These are: the large-scale meridional overturning (and its dependence on the diapycnal mixing in critical small-scale regions), the near-bottom circulation (in particular the strength and path of the Deep Western Boundary Current (DWBC)), and the ventilation of the thermocline (subduction in the eastern basin) (Willebrand et al., 2000). It turns out that the representation of boundary layer physics is generally important, e.g., the entrainment in overflows determines the overturning circulation and requires the right amount of iso- and diapycnal mixing as well as along-bottom advection.

The DAMEE-NAB (Data Assimilation and Model Evaluation Experiments-North Atlantic Basin) project is the latest of these model intercomparison projects. Funded by the Office of Naval Research, the overall goal of the DAMEE program has been the development of a global ocean nowcasting capability with basin-wide forecasting skill that provides descriptions of the three-dimensional ocean structure, the locations of mesoscale features such as eddies and ocean fronts, and environmental definition with accuracy superior to climatology and persistence. Technical objectives of DAMEE-NAB include systematic sensitivity studies with prognostic ocean models of varying design, the evaluation of their behavior via model–model and model–data comparisons, and the assessment of improvements in model skill made possible with model/data assimilation.

Here we present and discuss the first prognostic basin-scale solutions obtained with the Regional Ocean Modeling System (ROMS), a free-surface, finite difference model based on the nonlinear terrain-following coordinate of Song and Haidvogel (1994). Our objectives are twofold. First, we wish to assess the quality of the new terrain-following model in the limit of realistic basin-scale simulations, with particular emphasis on the utility of its nonlinear terrain-following coordinate and higher-order advection scheme. Second, we aim to compare the results obtained with ROMS against those of other

models used in DYNAMO and DAMEE. The emphasis herein is on an assessment of the fidelity of the time-mean and eddy (RMS variability) fields produced by the new terrain-following model. An accompanying manuscript (Malanotte-Rizzoli et al., 2000) considers issues related to seasonal cycling and water mass pathways.

The plan of the paper is as follows. The terrain-following model applied in the present study is described in Section 2, and the experimental configuration in Section 3. Section 4 presents the results from the central experiment. Seven sensitivity experiments and their quantitative assessment are reported in Section 5. A concluding section offers summary thoughts on the status of realistic modeling of the NAB.

## 2. Model description

The concept of terrain-following (or sigma) coordinates was first introduced in atmospheric modeling (Phillips, 1957) and has since become a standard alternative in large-scale and regional ocean circulation modeling (Haidvogel and Beckmann, 1998). Our terrain-following model hierarchy originated with the semi-spectral primitive equation model (SPEM; Haidvogel et al., 1991), which solves the hydrostatic, primitive equations subject to a rigid lid condition at the sea surface. Originally developed for high-resolution process studies, current versions of SPEM incorporate multiple thermodynamic and/or passive tracers, special masking features for islands and promontories, and a staggered finite difference treatment in the vertical coordinate, thereby allowing a wide range of regional and basin-scale studies (Hedström, 1994).

An algorithmically compatible free sea surface model (SCRUM, the S-Coordinate Rutgers University Model) was originated by Song and Haidvogel (1994). A valuable feature, first introduced in SCRUM and then retrofitted into SPEM, is a generalized nonlinear terrain-following coordinate which can be configured to provide enhanced resolution at either the sea surface or sea floor. The newest free surface model in this hierarchy, the ROMS, is an expanded version of SCRUM with a variety of new features, including alternatives for high-order upstream-biased advection, for subgrid-scale parameterization, and for high performance computing on SMP-class computer architectures. A brief description of the ROMS model is given next.

### 2.1. Equations of motion in transformed coordinates

With an active sea surface, a generalized topography-fitting coordinate takes the form

$$s = s \left( \frac{z - \zeta(x, y, t)}{H(x, y) + \zeta(x, y, t)} \right) \quad -1 \leq s \leq 0,$$

where  $H(x, y)$  is the resting thickness of the water column and  $\zeta(x, y, t)$  is the instantaneous height of the sea surface. (In case of a linear relationship between  $s$  and  $z$ , the transformation is equivalent to the traditional  $\sigma$ -coordinate.) As an extension to standard terrain-following transformations, a nonlinear stretching of the vertical coordinate can be applied that depends on local water depth (Song and Haidvogel, 1994). This option can be used to generate a more uniform vertical resolution near the surface and

consequently a better representation of the mixed layer and thermocline. The transformation used in ROMS is:

$$z = h_s + (h - h_s)C(s)$$

where  $h_s$  is a constant to be chosen as a typical surface mixed layer depth, and

$$C(s) = (1 - \theta_b) \frac{\sinh(\theta s)}{\sinh(\theta)} + \theta_b \frac{\tanh[\theta(s + 1/2)] - \tanh(\theta/2)}{2 \tanh(\theta/2)}$$

For large  $\theta$ , the coordinate lines are more tightly confined to the surface; additionally, if  $\theta_b$  approaches 1, resolution at the bottom boundary is enhanced. An example of the resulting placement of vertical levels is shown in the next section.

In keeping with the design of SPEM and SCRUM, the ROMS circulation model is written in horizontal curvilinear coordinates, wherein the transformed coordinates are defined by the relations

$$(dS)_\xi = \left( \frac{1}{m} \right) d\xi$$

$$(dS)_\eta = \left( \frac{1}{n} \right) d\eta$$

where  $m(x, y)$  and  $n(x, y)$  are the scale factors which relate the differential distances ( $d\xi, d\eta$ ) to the physical arc lengths  $dS$  (See, for example, Arakawa and Lamb, 1977). Note that this general formulation of curvilinear coordinates includes Cartesian coordinates (by setting  $m = n = \text{constant}$ ) as well as spherical coordinates (which we use below) with

$$m \sim \frac{1}{R \cos \phi}, \quad n \sim \frac{1}{R}$$

where  $\phi$  is the geographical latitude and  $R$  is the mean radius of the Earth.

Under these horizontal and vertical transformations, and with  $H_z \equiv (\partial z)/(\partial s)$ , the hydrostatic primitive equations become:

$$\begin{aligned} \frac{\partial}{\partial t} \left( \frac{H_z u}{mn} \right) + \frac{\partial}{\partial \xi} \left( \frac{H_z u^2}{n} \right) + \frac{\partial}{\partial \eta} \left( \frac{H_z u v}{m} \right) + \frac{\partial}{\partial s} \left( \frac{H_z u \Omega}{mn} \right) - \left\{ \left( \frac{f}{mn} \right) + v \frac{\partial}{\partial \xi} \left( \frac{1}{n} \right) \right. \\ \left. - u \frac{\partial}{\partial \eta} \left( \frac{1}{m} \right) \right\} H_z v = - \left( \frac{H_z}{n} \right) \left( \frac{\partial P}{\partial \xi} + \frac{g \rho}{\rho_o} \frac{\partial z}{\partial \xi} + g \frac{\partial \zeta}{\partial \xi} \right) + \frac{H_z}{mn} (\mathcal{F}_u + \mathcal{D}_u) \end{aligned} \quad (1)$$

$$\begin{aligned} \frac{\partial}{\partial t} \left( \frac{H_z v}{mn} \right) + \frac{\partial}{\partial \xi} \left( \frac{H_z u v}{n} \right) + \frac{\partial}{\partial \eta} \left( \frac{H_z v^2}{m} \right) + \frac{\partial}{\partial s} \left( \frac{H_z v \Omega}{mn} \right) + \left\{ \left( \frac{f}{mn} \right) + v \frac{\partial}{\partial \xi} \left( \frac{1}{n} \right) \right. \\ \left. - u \frac{\partial}{\partial \eta} \left( \frac{1}{m} \right) \right\} H_z u = - \left( \frac{H_z}{m} \right) \left( \frac{\partial P}{\partial \eta} + \frac{g \rho}{\rho_o} \frac{\partial z}{\partial \eta} + g \frac{\partial \zeta}{\partial \eta} \right) + \frac{H_z}{mn} (\mathcal{F}_v + \mathcal{D}_v) \end{aligned} \quad (2)$$

$$0 = -\frac{\partial P}{\partial s} - \left( \frac{gH_z \rho}{\rho_0} \right) \quad (3)$$

$$\frac{\partial}{\partial t} \left( \frac{H_z T}{mn} \right) + \frac{\partial}{\partial \xi} \left( \frac{H_z u T}{n} \right) + \frac{\partial}{\partial \eta} \left( \frac{H_z v T}{m} \right) + \frac{\partial}{\partial s} \left( \frac{H_z \Omega T}{mn} \right) = \frac{H_z}{mn} (\mathcal{F}_T + \mathcal{D}_T) \quad (4)$$

$$\frac{\partial}{\partial t} \left( \frac{H_z S}{mn} \right) + \frac{\partial}{\partial \xi} \left( \frac{H_z u S}{n} \right) + \frac{\partial}{\partial \eta} \left( \frac{H_z v S}{m} \right) + \frac{\partial}{\partial s} \left( \frac{H_z \Omega S}{mn} \right) = \frac{H_z}{mn} (\mathcal{F}_S + \mathcal{D}_S) \quad (5)$$

and

$$\frac{\partial}{\partial t} \left( \frac{\zeta}{mn} \right) + \frac{\partial}{\partial \xi} \left( \frac{H_z u}{n} \right) + \frac{\partial}{\partial \eta} \left( \frac{H_z v}{m} \right) + \frac{\partial}{\partial s} \left( \frac{H_z \Omega}{mn} \right) = 0. \quad (6)$$

where  $(\xi, \eta)$  are scaled horizontal distances along the curvilinear coordinate lines;  $(u, v, \Omega)$  are the  $(\xi, \eta, s)$  components of vector velocity  $\vec{v}$ ;  $P(\xi, \eta, s, t)$ , the dynamic pressure ( $p/\rho_0$ ); and  $\mathcal{D}$  and  $\mathcal{F}$ , dissipative and forcing terms, if any. All other variables are used in their standard notation. The “vertical velocity” in this coordinate system,

$$\frac{\partial s}{\partial t} = \Omega(\xi, \eta, s, t) = \frac{1}{H_z} \left[ w - (1+s) \frac{\partial \zeta}{\partial t} - mu \frac{\partial z}{\partial \xi} - nv \frac{\partial z}{\partial \eta} \right],$$

includes both “upwelling” and “upsloping” components of the vertical movement. In the transformed coordinate system, the kinematic boundary conditions at the surface ( $s = 0$ ) and the bottom ( $s = -1$ ) become:

$$\Omega = 0.$$

Lastly, the full UNESCO equation of state is implemented in a vectorized form, with modified coefficients for use with potential rather than in-situ temperatures (Jackett and McDougall, 1995).

## 2.2. Discretization and pressure gradient issues

In the horizontal directions  $(\xi, \eta)$ , a centered second-order finite-difference approximation is adopted (an Arakawa “C” grid; Arakawa and Lamb, 1977). Lateral boundary condition options include free-slip, no-slip and “partial-slip” walls (Haidvogel et al., 1992), as well as a variety of options for regional (open) boundary conditions. A second-order, staggered stencil is used in the  $s$ -coordinate. These choices are traditional for second-order, finite differences models, and provide for conservation of (e.g.) the first and second moments of momentum and tracers. Except where noted below, discretization procedures follow those outlined in Song and Haidvogel (1994) and Hedström (1997).

The terrain-following coordinate system, when discretized, is subject to a special systematic error, associated with the possibility of significant errors in the horizontal pressure gradients (Haney, 1991; Beckmann and Haidvogel, 1993; Mellor et al., 1994). These errors arise due to the splitting of the pressure gradient term into an “along-coordinate surface” component and a “hydrostatic correction”. The latter term is necessary to remove that portion of the pressure variations along the sloping  $s$ -surfaces which are due to vertical hydrostatic pressure changes (which do not vary horizontally and hence do not accelerate the fluid). Unfortunately, both terms are large, and cancellation of the hydrostatic resting pressure is not exact, due to non-cancelling approximation errors in the two terms. The pressure gradient errors that result depend on the steepness of the topography, both the horizontal and vertical resolution, and the strength of the stratification.

Various methods have been proposed to reduce these errors, e.g., by applying the pressure gradient force only to the dynamically active deviation from a domain-wide reference profile  $\bar{p}(z)$  (Gary, 1973), and by using higher-order finite difference approximations in the horizontal (McCalpin, 1994; Chu and Fan, 1997). Despite these corrective measures, experience has shown that some degree of topographic smoothing may be necessary to ensure stable and accurate simulations using realistic bathymetry. For ROMS, a useful parameter is found to be

$$r = \frac{\Delta h}{2h} = \frac{h^{+1/2} - h^{-1/2}}{H^{+1/2} + H^{-1/2}} \quad (7)$$

(Beckmann and Haidvogel, 1993). Empirical studies have shown that robust results are obtained if  $r$  does not significantly exceed a value of 0.2.

### 2.3. Temporal discretization and mode coupling

The overall time-stepping scheme follows now standard procedures for primitive equation models. The baroclinic (depth-varying) modes of the velocity distribution are obtained by direct time stepping of the momentum equations, having removed their depth-averaged component. The free surface in ROMS is advanced in time explicitly with a much smaller time step (split-explicit time stepping). Implicit vertical diffusion is available for cases where the water depth is very small or where convection is parameterized by locally increased vertical diffusivity and/or viscosity.

A second-order accurate in space, centered advection scheme in combination with an Adams–Bashforth time step has been used previously in SCRUM. This choice has several disadvantages. Most importantly, the height of the fluid column is determined from the shallow water equations, which are advanced on a separate shorter time step. Consequently, it is difficult to build an advection scheme for tracers which is simultaneously *conservative* and *constancy-preserving*. To address these issues, we have redesigned the barotropic–baroclinic mode coupling mechanism to ensure that the continuity equation is satisfied *exactly* on the discrete level. The resultant time stepping algorithm is equivalent to a Leap-Frog — Adams–Moulton predictor–corrector scheme,

which is formally third-order accurate in time and has excellent dispersive properties for the advection equation up to the limits of temporal stability (Shchepetkin and McWilliams, 1998). Though formally the same order of accuracy as an Adams–Bashforth time step, this combined approach reduces formal truncation error by approximately one order of magnitude, which offsets the increased computational cost.

#### *2.4. Subgrid-scale closure*

Several horizontal mixing operators in curvilinear coordinates are implemented in ROMS, including harmonic (Laplacian) and biharmonic forms for viscosity and diffusivity. The associated mixing coefficients for momentum and tracers can either be constants, grid-size-dependent, or time-varying (proportional to the properties of the flow field). Diffusion along  $s$ -surfaces, although numerically the most convenient choice, mixes tracer properties from different depths. The vertical mixing thus introduced by the lateral mixing operator can exceed the desirable value of diapycnal mixing. Therefore, the ability to re-orient the mixing tensor along other orientations (geopotential or isopycnal/epineutral) is essential. In ROMS, both harmonic and biharmonic tensors (for momentum and tracers) can be rotated.

The need for finite levels of quasi-horizontal smoothing of momentum and/or tracers can be met by either explicit incorporation of horizontal mixing terms (such as those just noted) or through the use of upstream-weighted advection schemes which effectively contribute varying degrees of implicit smoothing. In the simulations reported below, the third-order upstream (TOUS) advection scheme of Shchepetkin and McWilliams (1998) is used throughout, except where noted. This advection scheme is associated with weak, fourth-order (biharmonic) smoothing which was found to be sufficient by itself to produce well-behaved solutions. Hence, no explicit horizontal viscosity or diffusivity was needed in these cases.

Parameterization of surface mixing follows the K-profile parameterization of Large et al. (1994). The resulting vertical mixing can be time-stepped either explicitly, or semi-implicitly using a Crank–Nicholson scheme with equal weights for the old and new time steps. The latter leads to a standard tri-diagonal system of equations. Options for instantaneous convective adjustment are also available in ROMS, though they were not employed in the simulations reported below.

#### *2.5. Parallel performance*

ROMS has been optimized for the SGI PowerChallenge and the CRAY Origin 2000 architectures, with the potential of porting it to the CRAY T3E. This redesign includes the introduction of explicit two-dimensional partitioning (blocking) into subdomains, which can be assigned to different processors. In this code the number of subdomains is not necessarily equal to the number of processors used. Instead we may elect to make each processor work on several subdomains, while the subdomain size is chosen for optimal use of the processor cache. The sustained single-processor performance of this code is approximately 125 MFlops on the CRAY Origin 2000, with an estimated performance of 3.2 Gflops on 32 processors. The resulting  $3/4^{\circ}$  North Atlantic model

requires approximately 10 wall-clock hours on 16 SGI Origin processors to complete a 10-year simulation on the full-domain grid described next.

### 3. Description of experiments

The geographical domain selected for the model/model comparison phase of DAMEE-NAB is the NAB between 6°N and 50°N. Bathymetry data was derived from the ETOPO-5 (5 min) gridded dataset (National Geophysics Data Center, 1988). Surface forcing functions were drawn from the COADS climatology of Da Silva et al. (1994). These forcing fields included surface wind stresses, heat and freshwater fluxes, and heat flux sensitivity to sea surface temperature. The latter is used to represent the feedback between model SST and the surface heat flux (Da Silva et al., 1994). Buffer zones are applied at the northern and southern boundaries (3° wide in either case) and in the Gulf of Cadiz to emulate interbasin exchange processes. In these nudging zones, temperature and salinity are relaxed to observed monthly T and S (climatology) with relaxation times of 5 days at the domain boundaries increasing to 60 days at the interior edge of the buffer zone. No-slip lateral boundary conditions are applied on all solid sidewalls. Lastly, initial conditions for the DAMEE simulations are obtained from either the NAVOCEANO Generalized Digital Environmental Model (GDEM; [http://128.160.23.42/gdemv/gdem\\_desc.html](http://128.160.23.42/gdemv/gdem_desc.html)) or the Levitus climatology (Levitus and Boyer, 1994; Levitus et al., 1994). The latter was used below.

Following these specifications, a series of simulations using ROMS has been conducted to explore parameter sensitivities known to be of importance in determining model fidelity. Given the experience in CME and DYNAMO, the parameter sensitivities identified for study included horizontal and vertical resolution, vertical coordinate treatment (as represented here by the degree of surface stretching, i.e., the value of  $\theta$ ), domain size, the surface boundary condition used for salinity, and the treatment of three-dimensional advection. Table 1 summarizes the attributes of the eight simulations in this sequence.

Table 1

Table of experiments. Experiments are identical to E1 unless otherwise noted

Experiment	Domain	Topography	$\Delta x$	$\theta$	N	Surface BC	Advection	$\nu, k$
E1	30°S–65°N	T1	3/4°	5	20	(E–P)	TOUS	0,0
E2				0				
E3					40			
E4						relaxation		
E5	6°S–50°N							
E6		T2	3/8°			relaxation		
E7							2nd-order centered	$6 \times 10^{12}$ , $2 \times 10^{12} \text{ m}^4/\text{s}$
E8							4th-order centered	$6 \times 10^{12}$ , $2 \times 10^{12} \text{ m}^4/\text{s}$

Of the eight experiments, the first (hereafter, E1) utilizes an oceanic grid which spans the latitude range 30°S to 65°N (Fig. 1a). Vertical resolution, dictated by DAMEE consensus, is 20 sigma levels ( $N = 20$ ). The non-eddy-resolving horizontal resolution used in E1 ( $3/4^\circ$ ) is chosen to be intermediate between the values used in DYNAMO and the DAMEE small-domain intercomparison experiment described elsewhere in this volume. The  $s$ -coordinate parameters ( $\theta = 5$  and  $\theta_b = 0.4$ ) were based upon prior experience (e.g., DG97) which showed some degree of coordinate focusing near the top and bottom to be desirable (A cross-section of the vertical coordinate lines along 27°N is shown in Fig. 2). This configuration is similar to that used in other studies using SPEM and SCRUM (e.g., Barnier et al., 1998).

With horizontal resolution held fixed at  $3/4^\circ$ , six additional experiments (labeled E2–E5, E7, E8) were performed to investigate the influences of alternate vertical discretizations, surface boundary conditions, domain size, and advection algorithm. Experiment 2 replaces the stretched vertical coordinate of E1 ( $\theta = 5$ ) with a pure sigma coordinate ( $\theta = 0$ ). (Uniform spacing in the resulting “vertical” coordinate is used, resulting in second-order treatment in both cases). Experiment 3 assesses sensitivity to vertical resolution by increasing the number of vertical  $s$ -levels to 40. The fourth simulation (E4) explores the influence of surface salt flux boundary conditions by replacing salt fluxes based on COADS (E–P) measurements with a simple relaxation to Levitus surface salinity climatology (time scale = 50 days). Experiment five (E5) contrasts the results obtained in the extended domain of E1–E4 (30°S to 65°N) with those produced in the smaller DAMEE-consensus domain (6°N to 50°N; Fig. 1). The plausible rationale for the selection of the smaller domain is computational economy; however, the fictitious “open boundaries” are now located much closer to the region of interest, and the influence of this placement requires examination. Lastly, the impact of the TOUS scheme for tracer advection is assessed in experiments E7 and E8 which

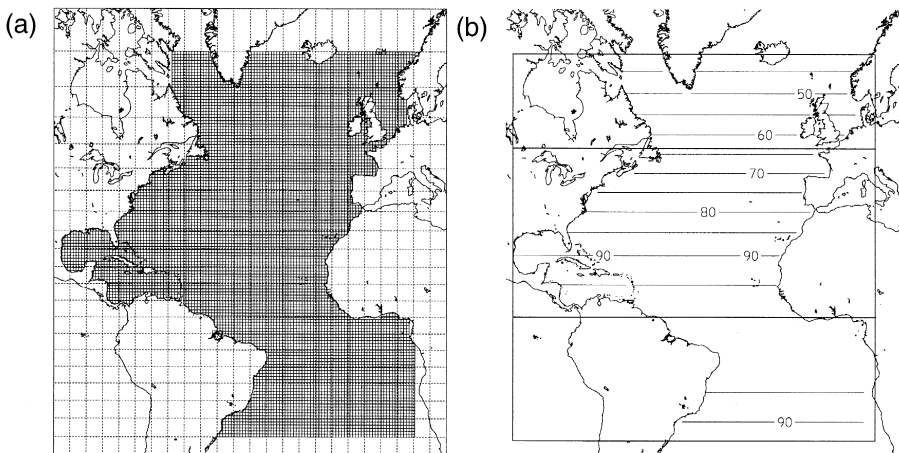


Fig. 1. Grid and grid spacing for the  $3/4^\circ$  experiments described in Table 1: (a) grid, (b) meridional spacing (km). The inner boxed region in (b) corresponds to the DAMEE consensus domain.

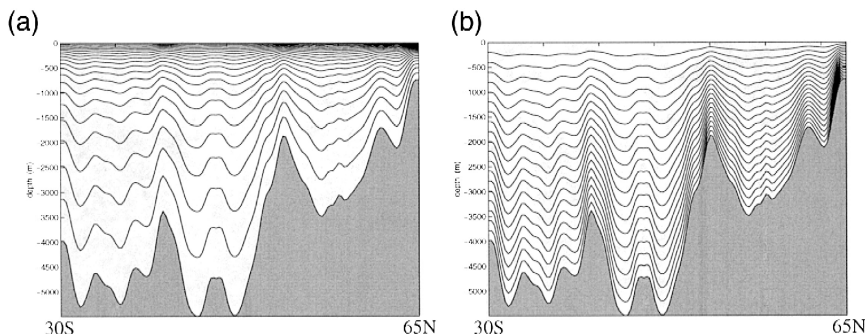


Fig. 2. Sections along 30°W showing vertical coordinate surfaces used in the experiments ( $N = 20$ ): (a)  $\theta = 5$ , (b)  $\theta = 0$ .

utilize second- and fourth-order, centered advection algorithms (for both momentum and tracers), respectively, along with a modest amount of biharmonic, geopotentially rotated viscosity and diffusivity (Table 1).

At a horizontal resolution of only  $3/4^\circ$ , we anticipate that some processes will be under-resolved, if not absent altogether. These processes include eddy generation related to internal instabilities (e.g., baroclinic instability), eddy-topography interactions, the formation of inertial gyres, and (possibly) western boundary current separation. The latter is of particular interest. For example, several prior studies did not obtain satisfactory Gulf Stream separation until sufficient horizontal resolution, in the neighborhood of 10 km, was attained. To explore sensitivities to enhanced horizontal resolution, we have conducted an additional experiment at a nominal resolution of  $3/8^\circ$  (E6). It is identical to E1 except for horizontal grid (subdivided by a factor of two in each horizontal direction), and underlying topography (which requires less smoothing at this enhanced resolution).

The bathymetry on the model grid was obtained by bi-linear interpolation of the ETOPO5 data. Depths shallower than 200 m were reset to 200 m, and abyssal depths to a maximum value of 5500 m (Shallower continental shelves were not found to significantly influence model behavior at the resolution used here). After interpolation and truncation, the topography was smoothed using a Shapiro-based filter which acts selectively in regions wherein the “ $r$ -factor” (Eq. (7)) exceeds the value of 0.2. The filter is known to cause shallow shelves to disappear into the land mask, so between applications of the filter the shallow shelves were lifted back up to 200 m. The resulting topographies, called T1 and T2, are shown in Fig. 3.

For the tracer fields, the initial conditions and monthly climatologies (the latter used in nudging zones adjacent to the northern and southern “open” boundaries) were derived from the Levitus and Boyer (1994) and Levitus et al. (1994)  $1^\circ$  resolution dataset and interpolated to the model grid via objective analysis. An analytical, isotropic, Gaussian correlation was used for the mapping with a decorrelation scale of 300 km. The fields were mapped to the same vertical levels as in the Levitus dataset, and then vertically interpolated using cubic splines to the terrain-following coordinate grid. The

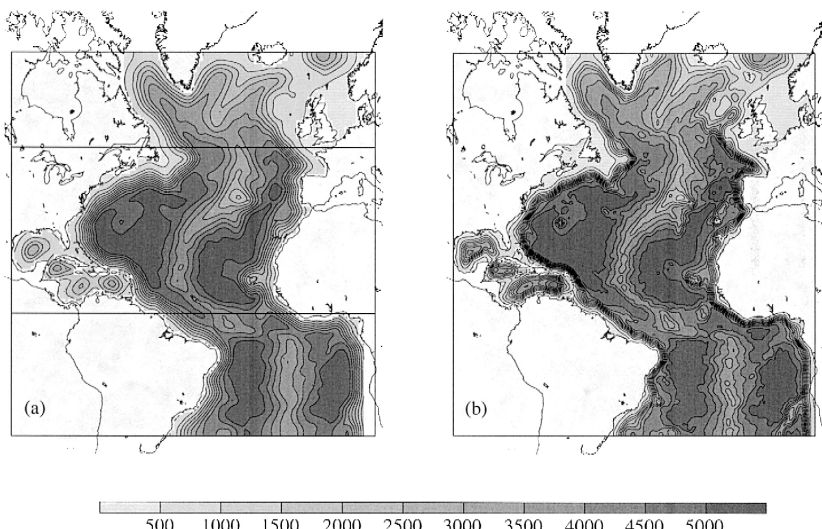


Fig. 3. Bathymetry (in meters) for the experiments described in Table 1: (a) E1, (b) E6.

February monthly climatology was selected for initialization. The forcing fields were mapped from the COADS  $1^{\circ}$  resolution dataset (Da Silva et al., 1994) in a similar fashion.

Clearly, other parametric and numerical choices may be consequential to model realism. Nonetheless, in the interests of a tractable series of parameter variations, certain physical and numerical choices have been held fixed over the course of the experiments listed in Table 1. The most important of these are the surface mixed layer algorithm (the KPP scheme is used throughout) and the surface forcing datasets (COADS). The baroclinic timesteps, chosen to produce stable integration across model runs, were 5400 and 2700 s, respectively, for the low- and higher-resolution experiments; there were 27 barotropic timesteps per baroclinic step (i.e., timesteps of 200 and 100 s, respectively).

#### 4. Central experiment

We first review the basic properties of experiment E1, chosen as that experiment of our sequence with the most “traditional” set of parameter values. As we discuss below, E1 is not the most successful experiment by all measures; however, its results are broadly representative of the behavior we have found for ROMS. For the purpose of evaluation, we emphasize wherever possible either known observational measures and/or equivalent diagnostic measures obtained from DYNAMO (DG97) and DAMEE/MICOM (Paiva et al., 2000; hereafter, PCM00).

##### 4.1. Spin-up and long-term drift

A time series of volume-integrated kinetic energy per unit area (i.e., units of Joules per square meter) is shown in Fig. 4. The central ROMS experiment (E1) exhibits a

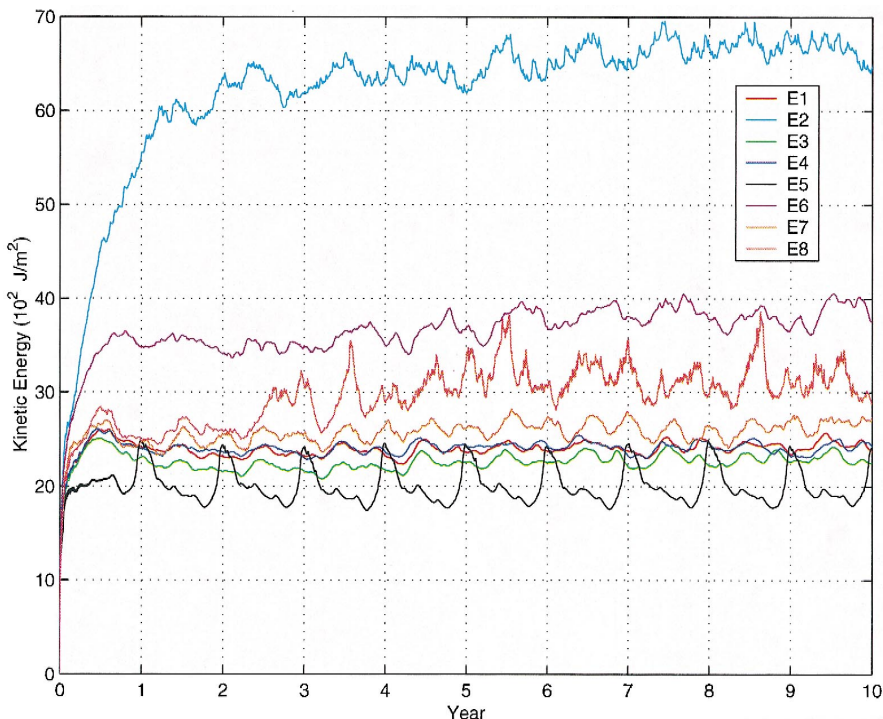


Fig. 4. Time series of column-averaged kinetic energy (volume-integrated kinetic energy divided by surface area).

rapid rise in kinetic energy, followed (after approximately 1 year) by small temporal variations about an equilibrium value of about  $2400 \text{ J/m}^2$ . Little temporal trend in mean kinetic energy level is apparent in the time series; continuation of the experiment to year 20 confirms this visual impression. ROMS displays little in the way of an obvious seasonal cycle in KE. The dominant temporal fluctuations in E1 (and in all the large-domain experiments) appear to be semi-annual in period, with an amplitude about the mean level is small of approximately  $100\text{--}200 \text{ J/m}^2$ . The results of experiments E2–E8 are discussed below in Section 5.

Similar KE estimates are not available from observations. Comparable estimates from MICOM (PCM00, Fig. 1) show a similar initial rise in KE level, followed by a weak but noticeable adjustment on an approximate 5-year time scale. Equilibrium is reached by year 10 in the MICOM cases, corresponding to bulk KE values of approximately 1300 and  $2500 \text{ J/m}^2$ , respectively, for their  $1^\circ$  and  $1/2^\circ$  experiments, respectively. A stronger (amplitude of  $300 \text{ J/m}^2$ ) and more coherent annual cycle in KE level is found in MICOM when compared with that obtained in E1. ROMS is thus more energetic than MICOM — the  $3/4^\circ$  ROMS experiment having very nearly the same overall energy level of the  $1/2^\circ$  MICOM simulation — but has a less distinguished annual cycle of kinetic energy.

An important measure of model fidelity is the degree to which it is able to preserve the bulk (i.e., globally averaged) values of its tracer fields. Fig. 5 shows time series of the volume-averaged values of temperature and salinity for the 10 years of the ROMS

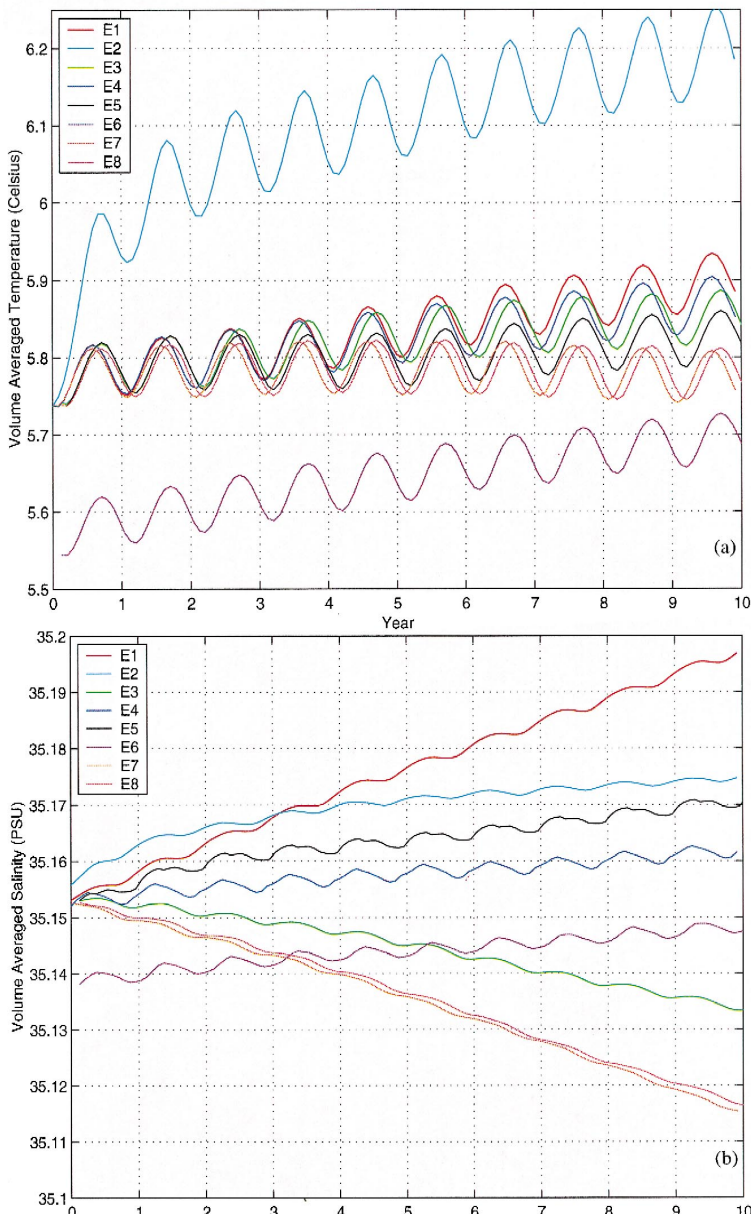


Fig. 5. Time series of volume-averaged tracer values between 9°N and 47°N: (a) temperature, (b) salinity.

central experiment. Both bulk quantities show an increase in time, with little indication of an approach to an equilibrium value over the 10-year record. Volume-averaged temperatures show a yearly increase of approximately  $0.015^\circ/\text{year}$ ; the corresponding rate of salinity rise is close to  $0.004 \text{ PSU}/\text{year}$ . The spatial distribution of these tracer drifts is discussed further below.

These secular increases in temperature and salinity are typical of today's coarse-resolution, basin-scale simulations. Insofar as the Levitus initial fields are truly representative of the "correct" equilibrium values, and so long as these trends are not part of some unresolved long-time-scale variability, then these departures from climatology are likely caused by the mismatch between initial hydrography and surface forcing fields. For comparison the equivalent drifts from MICOM (PCM00, Fig. 3) are  $0.03^\circ/\text{year}$  and  $0.0025 \text{ PSU}/\text{year}$ . Thus tracer fields in the ROMS central case drift more slowly in temperature, but more rapidly in salinity, than do the MICOM results. Note also that the rate of drift in the MICOM bulk temperature values is beginning to slow by year 10, whereas the rate of increase in ROMS remains steady.

Many factors no doubt play a role here. A potentially important difference between the two models is that ROMS, unlike MICOM, has two prognostic variables for temperature and salinity. (Outside of the surface mixed layer, temperature values in MICOM are obtained from salinity, given the specified layer density.) Whether or not this issue is predominant here is unknown. Other factors in tracer evolution are likely to be consequential as well. For example, the relative effectiveness of tracer nudging layers is known to be dependent on model formulation (Killworth, 2000).

#### *4.2. Time-mean water mass structure*

The time-mean vertical profiles of area-averaged temperature and salinity are shown in Fig. 6, where an average over the last 3 years (8–10) has been taken. The interest in these diagnostics is to determine at what level(s) in the water column the anomalous heat and salt have been deposited over the course of the central experiment. As seen in Fig. 6, the anomalous values of temperature and salinity have differing vertical distributions. There is negligible drift in temperature at both the surface (depths less than about 800 m) and in the deep ocean (below 2500 m); the majority of the temperature increase is, in the area average, occurring at mid-depth ( $-2000 \text{ m} \leq z \leq -800 \text{ m}$ ). At these levels, the maximum temperature increase is approximately  $0.4^\circ\text{C}$ . By contrast, the positive salinity anomalies are occurring primarily in the upper 1000 m, with only small, oscillating departures from climatology below this. Maximum anomalies occur near the surface, and are of substantial ( $0.5 \text{ PSU}$ ) amplitude. [As we show below, this behavior is related to excessive salt input due to the surface (E–P) boundary condition.]

PCM00 also tabulate their area-averaged vertical tracer profiles (their Fig. 4), and the following contrasts are noted. In the upper water column ( $-1000 \text{ m} \leq z$ ), both models acquire an excess of salt. The MICOM simulations tend to depart less rapidly from the Levitus salt climatology, accounting for the overall slower bulk salinity drift noted above. However, MICOM's near-surface temperatures have also increased modestly, in contrast to the ROMS results. In the lower thermocline, ROMS experiences nearly the entirety of its anomalous heating, whereas MICOM displays little systematic temperature drift in the range  $-2000 \text{ m} \leq z \leq -1000 \text{ m}$ . Lastly, MICOM has a noticeable

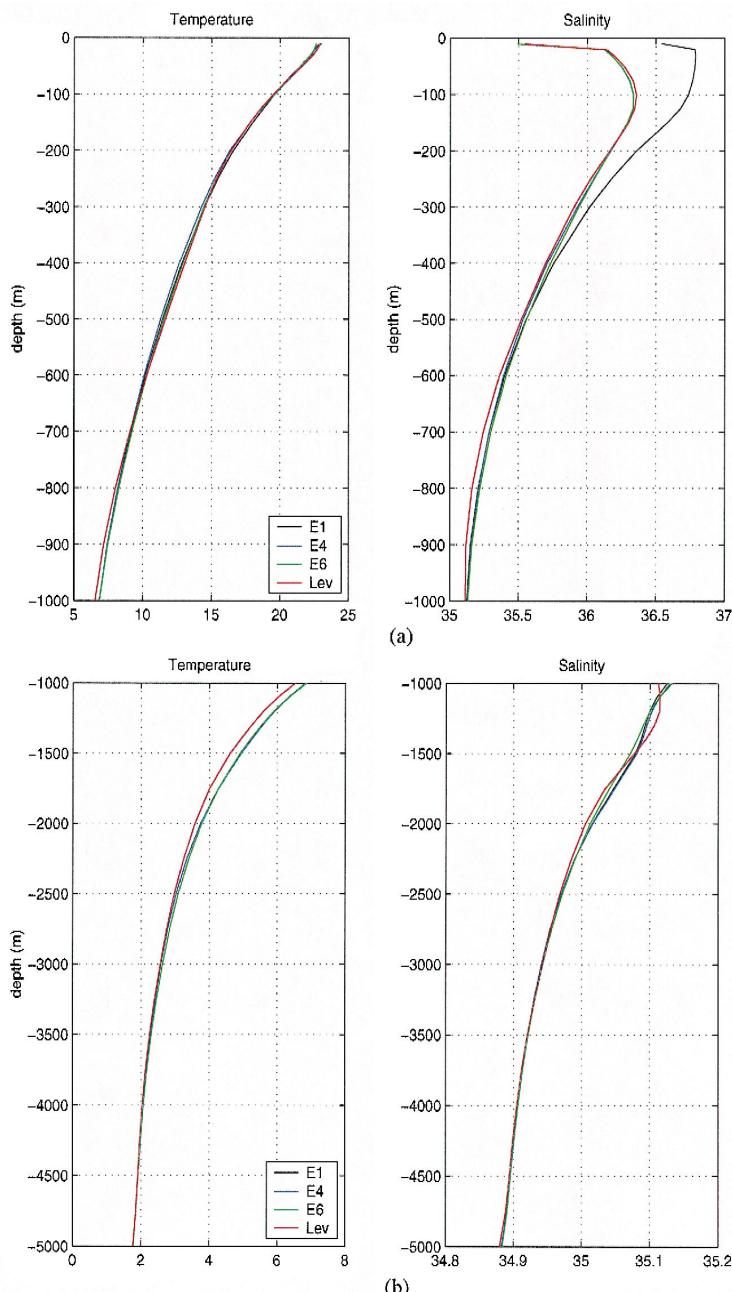


Fig. 6. Area-averaged temperature ( $^{\circ}\text{C}$ ) and salinity (PSU; black, blue, and green are the model average over the last 3 years; red is Levitus and Boyer (1994): (a)  $-1000 < z < 0$ , (b)  $-5000 < z < -1000$ .

increase in both temperature and salinity in the deep ocean (below 2500 m), while ROMS continues to track Levitus quite closely, at least up to year 10.

Closer inspection of the temperature and salinity anomalies in E1 reveals heterogeneous horizontal spatial structure in each. For example, temperature anomalies along the 55°W and 30°W meridians are shown in Fig. 7. In the western basin (Fig. 7a), the anomalous temperature structure at years 8–10 is dominated by narrow bands of cold (warm) water to the south (north) of approximately 42°N, with maximum amplitudes of about  $\pm 5^{\circ}\text{C}$ . Since this is the approximate location of the Gulf Stream front, the anomaly patterns are suggestive of a southward shift in the mean axis of the Gulf Stream along this meridian (see below). The negative anomaly to the south penetrates more deeply (to 700 m) than does the positive expression to the north, suggesting some bias in the tilt of the Gulf Stream thermal front. By comparison, salinity anomalies along 55°W are dominated by a broad band of excess surface salinity at low latitudes, and a subsurface “tube” of excessive saline water to the north of the Gulf Stream front. A possible explanation for the subsurface excess of salt at 45°N is that anomalous fluxes of salt injected by the surface forcing at low latitudes are transported northwards by the western boundary current system. Another possibility is that the fresh slope waters expected at this latitude are not being properly produced by the model. We address these alternatives further below.

A rather different spatial picture of tracer anomaly distributions emerges along 30°W. Temperature anomalies (Fig. 7b) are mostly positive, particularly in the depth range  $-500 \text{ m} \leq z \leq -1000 \text{ m}$ . Salinity anomalies are weaker by a factor of five than those along 55°W and more highly structured. Taken together, the tracer anomaly patterns in the western and eastern basins suggest that the excess heating at mid-depth (cf., Fig. 5) is localized primarily in the eastern basin, while the ultimate source of the excess salinity is mainly confined to the low-latitude western Atlantic.

#### 4.3. Meridional circulation

The large-scale thermohaline forcing of the ocean leads to a global circulation driven by sinking in high latitudes. The important elements of this thermohaline circulation include deep convection, overflow processes, the continuous DWBC, abyssal spreading of water masses, and a more or less uniform upwelling. The Mediterranean Water, injected at mid-latitude on the eastern boundary, also plays a role in the thermohaline circulation, as it is believed that its influence is felt throughout the North Atlantic and especially in the formation region of North Atlantic Deep Water (NADW). Of these elements, we consider below those for which quantitative estimates are generally accepted, i.e., the zonally integrated overturning motion, the meridional flux of heat, and the resulting internal distributions of large-scale potential vorticity.

The meridional overturning streamfunction, a function of latitude and depth, is an important characteristic of the thermohaline circulation. It is computed from the elliptic equation

$$\left( \frac{\partial^2}{\partial \phi^2} + \frac{\partial^2}{\partial z^2} \right) \Phi = \left( \frac{\partial \bar{v}^\lambda}{\partial z} - \frac{\partial \bar{w}^\lambda}{\partial \phi} \right)$$

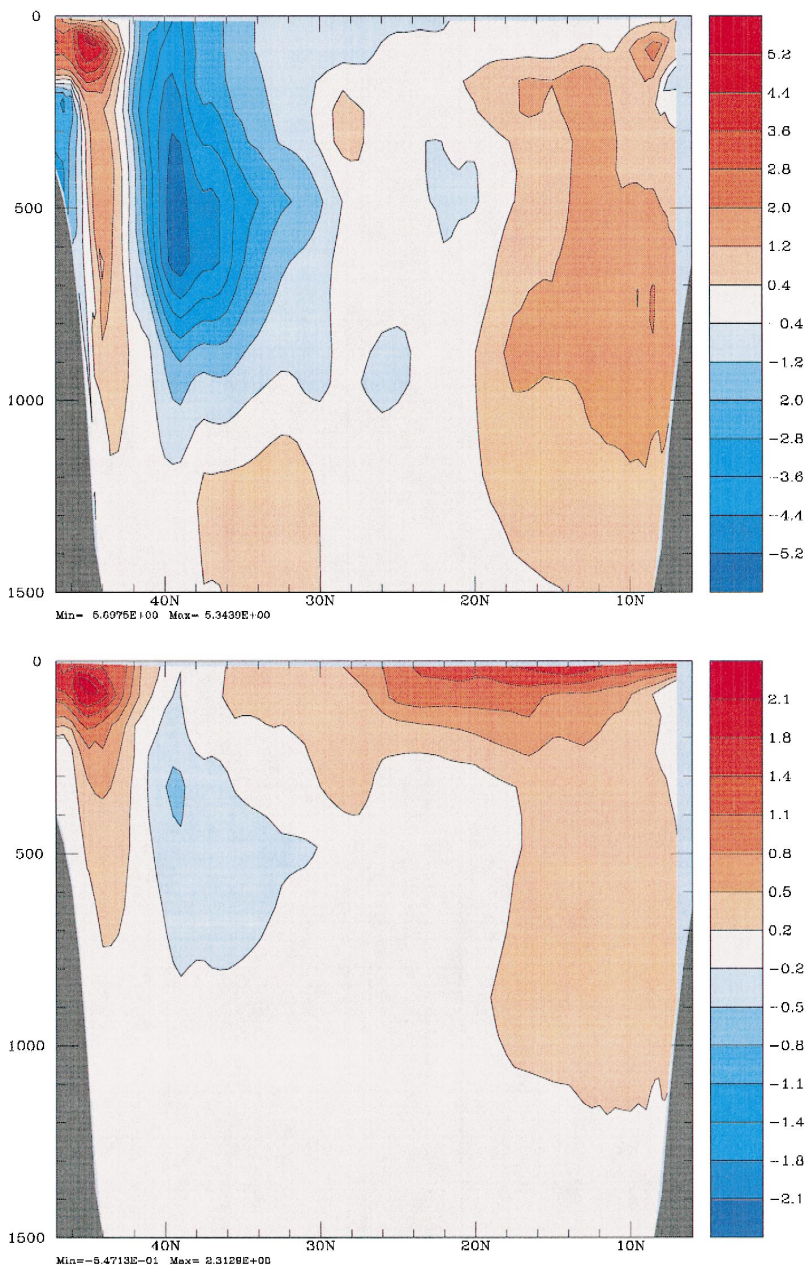


Fig. 7. (a) Time-mean temperature (C, upper) and salinity (PSU, lower) anomalies from Levitus along 55°W for E1. (b) Time-mean temperature (C, upper) and salinity (PSU, lower) anomalies from Levitus along 30°W for E1.

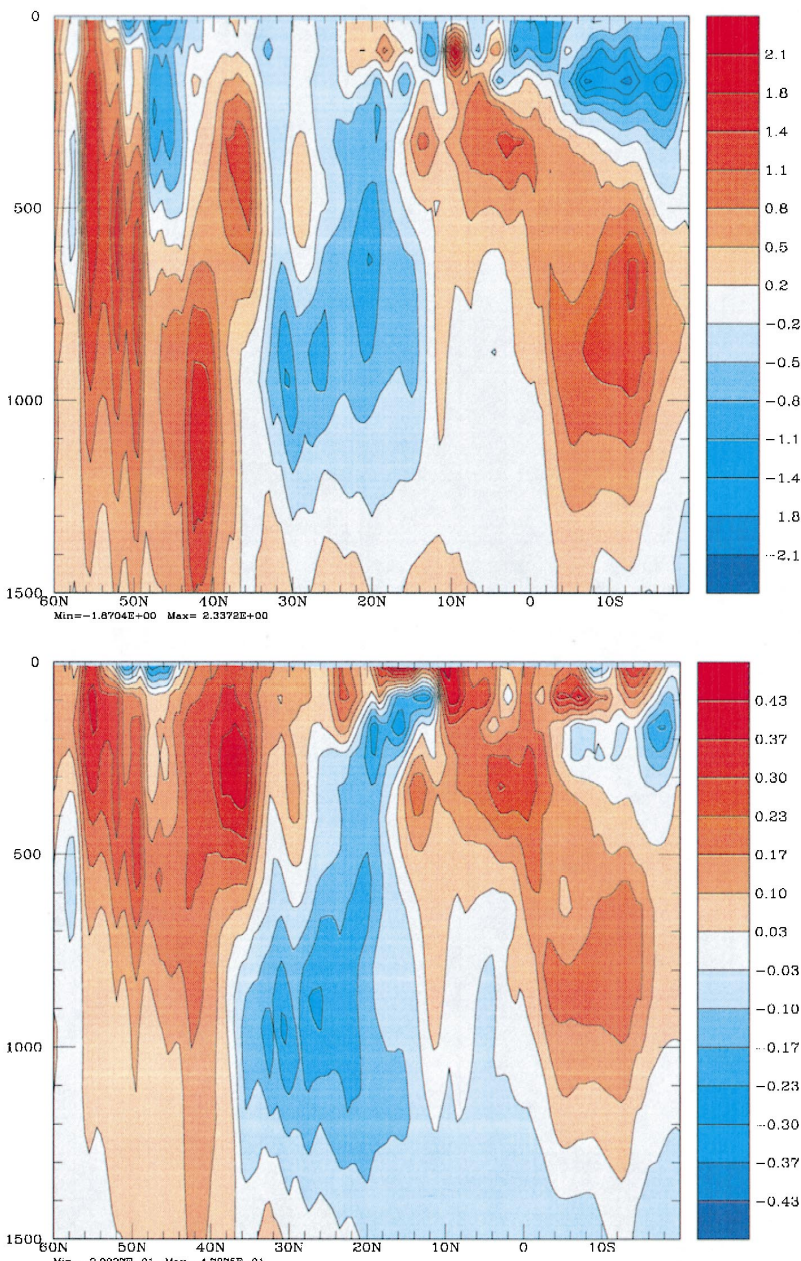


Fig. 7 (continued).

where the  $\overline{(\cdot)}^{\lambda}$  denotes the zonal average, or by integrating the meridional velocities zonally and vertically

$$\Phi(\phi, z) = \int_{-H}^z \left( \int_{\lambda_w}^{\lambda_e} v \, d\lambda \right) dz.$$

The large-scale overturning is not directly observable, but an annual mean maximum overturning of about 16–20 Sv between 40°N and 50°N in the depth range of 1000 to 1500 m seems consistent with estimates of the corresponding heat transport. Thus, we anticipate a large-scale structure of  $\Phi$  which is dominated by the NADW cell in the upper water column. Below, the counter-rotating Antarctic Bottom Water (AABW) cell transports 2–4 Sv.

The time-mean overturning circulation computed from E1 is broadly consistent with this picture (Fig. 8). The maximum overturning obtained in the central experiment is, in terms of its maximum amplitude (20 Sv), within available estimates. Maximum overturning occurs in the latitude band from 25°N to 30°N, at a depth of approximately 700 m, arguably shallower and south of observational inference. Relative to prior model simulations; however, these estimates are not atypical. Results from the DYNAMO experiment obtained using the SPEM sigma-coordinate model (DG97) show a nearly

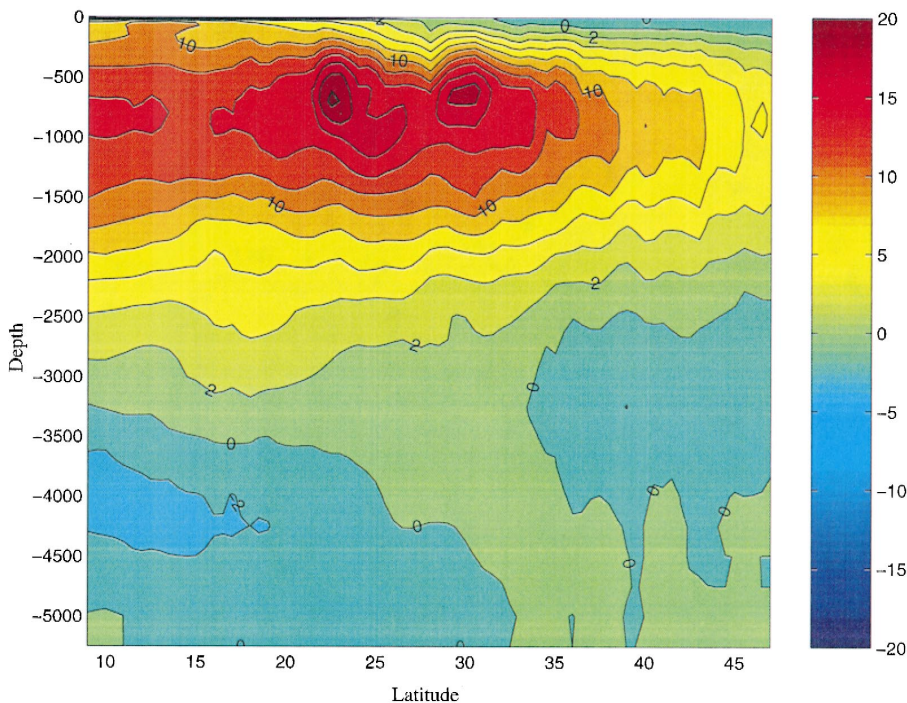


Fig. 8. Mean annual meridional overturning streamfunction for E1 (Sv).

identical maximum overturning rate, as well as latitudinal and vertical placement. It is noteworthy that the ROMS overturning streamfunction is considerably smoother than are prior results obtained with alternate sigma-coordinate models (e.g., DG97, Fig. 4.1c). It is possible that the relatively coarse horizontal resolution is a factor here, but as we show below the ROMS meridional overturning streamfunction is also smooth at finer resolution.

Directly linked to the meridional overturning circulation is the meridional transport of heat, a climatically important quantity for which independent estimates exist from both observations and atmospheric circulation models. The net meridional heat transport is defined as

$$HT(\phi) = \rho_o c_p \int_{-H}^0 \left( \int_{\lambda_w}^{\lambda_E} v \theta a \cos \phi d\lambda \right) dz$$

where  $c_p$  is the specific heat of sea water (taken to have the value  $4.06 \times 10^6 \text{ J/m}^3/\text{C}$ ). Curves of this quantity usually show a northward heat transport throughout the North Atlantic, with a maximum of about 1 PW between  $20^\circ\text{N}$  and  $40^\circ\text{N}$ , and 0.1 to 0.3 PW at the Equator [see, e.g., MacDonald (1995)]. The annual mean heat transport in the ROMS central experiment (Fig. 9) shows a broad maximum between about  $15^\circ\text{N}$  and  $25^\circ\text{N}$ ,

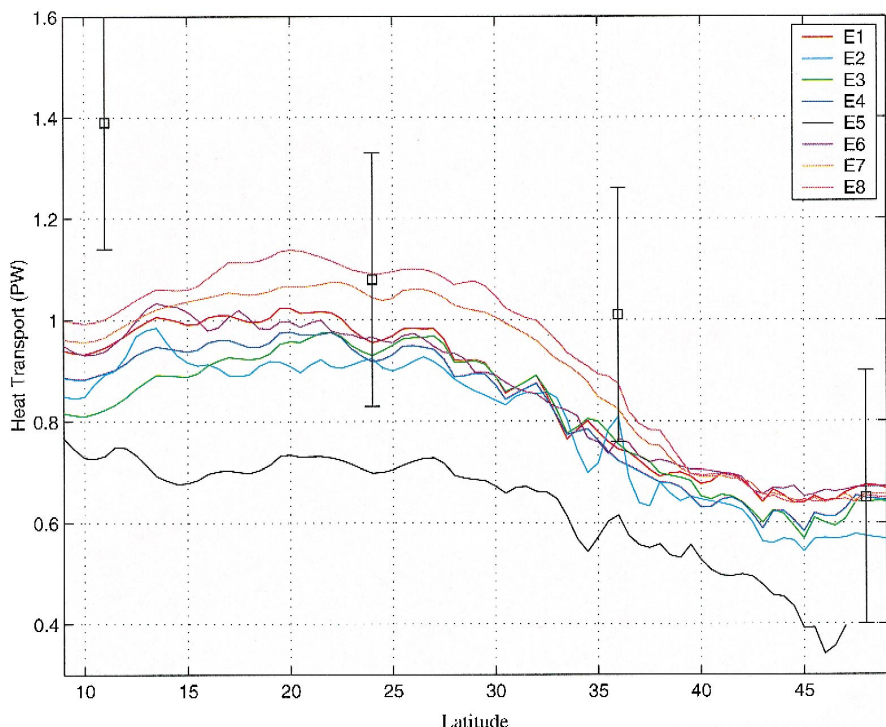


Fig. 9. Annual mean meridional heat transport (PW).

with an associated magnitude of about 1 PW, and diminished values at the Equator and farther north. These values are for the most part within accepted ranges, although the value at 10°N is outside the range of values posited by MacDonald and Wunsch (1996). This was true as well of all three models in the DYNAMO project (DG97), though the heat transport estimates from DAMEE/MICOM (PCM00, Fig. 8) are in better agreement at 10°N.

The large-scale potential vorticity, defined as

$$q = -\frac{1}{\rho_0} f \frac{\partial \rho}{\partial z},$$

can be used to study the formation of mode waters and subduction processes, and to identify regions of possible baroclinic instability. This quantity is often investigated on a section along 30°W, where it cuts through the Azores Current (at about 30°N) and the North Atlantic Current (at about 50°N). Observations (e.g., Robinson et al., 1979) show a bowl-shaped distribution of the potential vorticity, with local maxima at the position of the eastward flowing current bands.

In ROMS experiment E1 (Fig. 10) this overall structure of the potential vorticity is preserved between 10°N and 30°N. The near-surface maximum in the tropics can be followed northward at the base of the mixed layer. A deeper, secondary maximum exists at about 800 m in mid-latitudes. The major discrepancy with observations is the gap between the potential vorticity maximum related to the North Atlantic Current and the mid-latitude deep maximum, which is possibly an artifact of excessive mixing in the model. The Azores Current signature is very weak, as is common for non-isopycnic models at this resolution (Beckmann et al., 1994a; DG97).

#### 4.4. Gulf stream system

A recent overview on the subtropical western boundary circulation was given by Schott and Molinari (1996). Measurements of transport in the Florida Current indicate an annual mean mass transport of approximately 30–35 Sv. This mean transport is modulated by a seasonal cycle in transport of roughly 6 to 8 Sv. Fig. 11 (curve E1) shows the transport estimate of the central ROMS simulation. The 3-year average is about 34 Sv, with a 3 to 4 Sv seasonal signal (spring maximum and late fall minimum, in agreement with observations). This result also corresponds well to other (higher-resolution) models of the North Atlantic circulation. For example, the DYNAMO models (Willebrand et al., 2000) give a combined Florida/Antilles Current transport of 35–38 Sv, although they use a different wind product (ECMWF reanalysis data).

On its northward path, the simulated Gulf Stream transport increases to approximately 50 Sv downstream of its separation just south of Cape Hatteras. This separation of the Gulf Stream from the coast is not well represented in many non-eddy-resolving simulations of the North Atlantic. In general, the location of the Gulf Stream axis is too far north, hugging the coast all the way to Newfoundland. Better separation properties have been found in some simulations with terrain-following models at non-eddy-resolving resolution (e.g., Dengg et al., 1996), and with models at enhanced horizontal

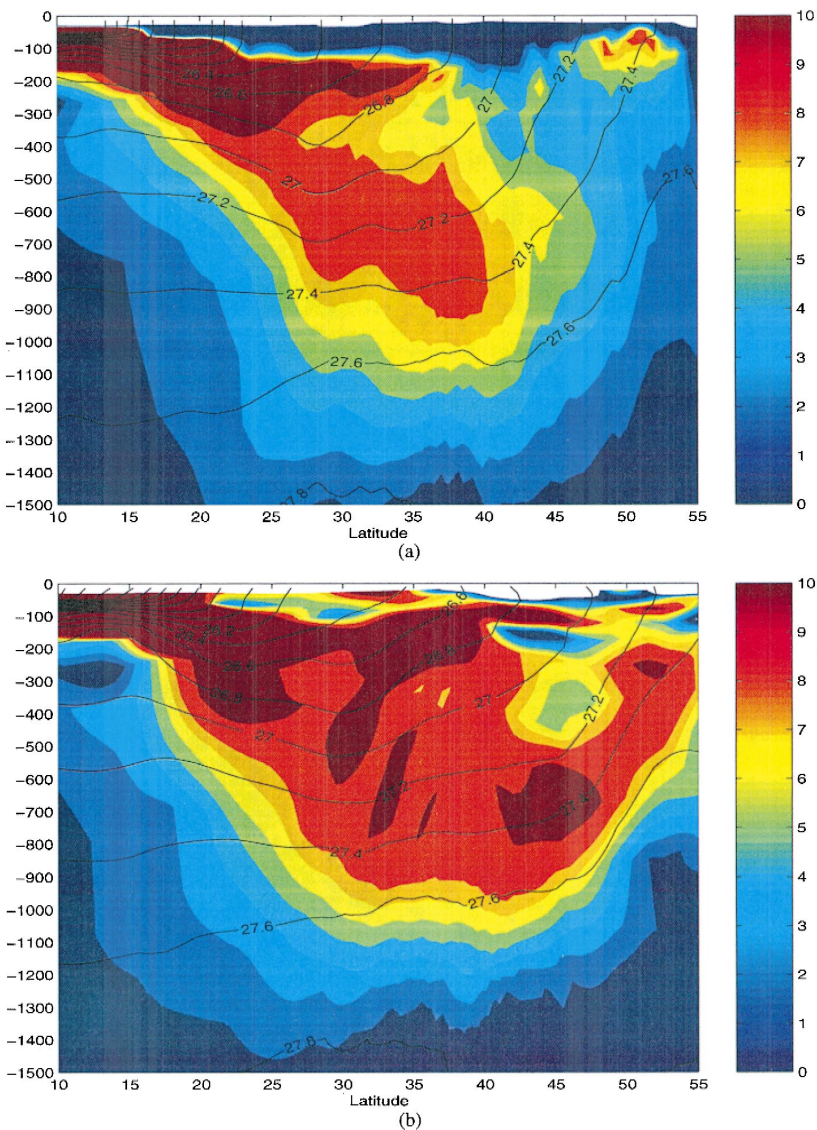


Fig. 10. Potential vorticity ( $10^{-11} \text{ m}^{-1} \text{ s}^{-1}$ ) for March along  $30^\circ\text{W}$ : (a) E1, (b) Levitus.

resolution (order 10 km; Smith et al., 2000; Paiva et al., 1999). Nonetheless, prior experience across model classes has been that proper separation is not obtained in general at non-eddy-resolving horizontal resolution.

In contrast to this prior experience, Gulf Stream separation in experiment E1 occurs at, or somewhat south of, Cape Hatteras rather than farther north. For example, Fig. 12 shows the monthly mean position position of the Gulf Stream axis (defined by the  $15^\circ\text{C}$

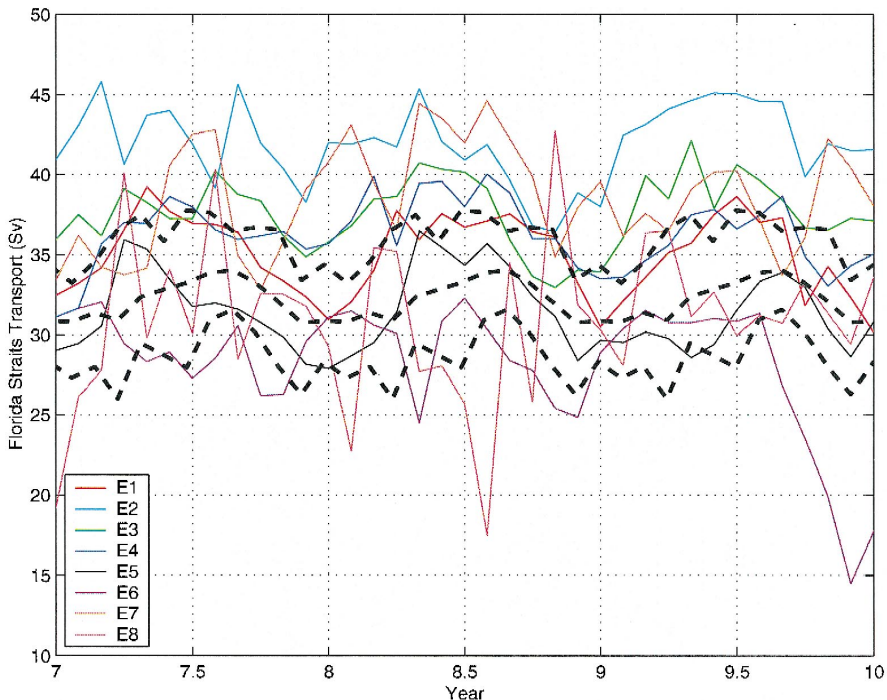


Fig. 11. Florida Strait transport (Sv). Black dashed lines are cable data at 27°N from J.C. Larsen.

isotherm in 200 m depth) for the last 3 years of experiment E1. The Gulf Stream path is generally satisfactory out to about 62°W, after which it lies too far south, possibly indicative of unrealistic interaction with the New England Seamounts. The ensemble of the frontal location shows seasonal and interannual variability, but no eddy activity which is prohibited by the coarse horizontal resolution. These separation properties are superior in some respects to those obtained in many prior studies at comparable resolution, as well as to those produced by other DAMEE groups (e.g., PCM00). Whether or not this result is somehow fortuitous is not entirely clear. Nonetheless, the sensitivity studies described below produce comparably realistic Gulf Stream separation, suggesting some degree of robustness to these ROMS simulations.

Results from the DYNAMO study (Willebrand et al., 2000) suggest that terrain-following models tend to have a stronger (arguably, perhaps, somewhat too strong) subpolar gyre, and a Gulf Stream separation affected by a strong southward excursion of the Labrador Current into the Mid-Atlantic Bight. The tendency for accentuated along-topography flows — possibly a consistent attribute of sigma coordinate models — may be playing a part in the improved separation properties of E1. The southward deflection of the Gulf Stream path at the longitude of the New England Seamounts is also suggestive of this effect.

In reality, the southward along-coast transport associated with the DWBC has a maximum of 10–15 cm/s at about 2000–2500 m depth. In a terrain-following model at

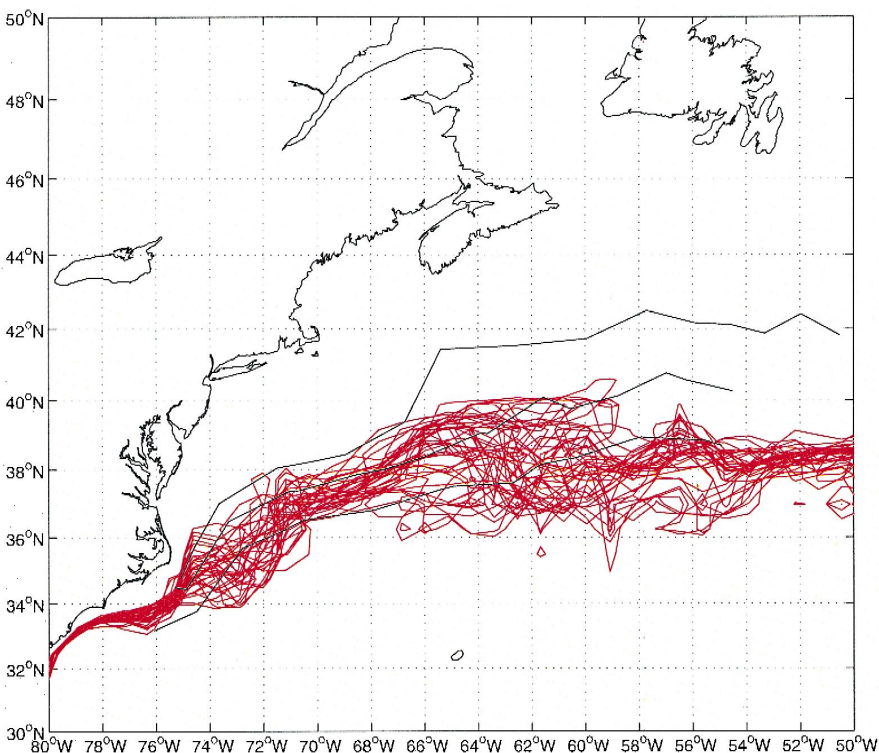


Fig. 12. Monthly means of the Gulf Stream north wall for years 8–10 from E1. The black lines are the TOPEX 1992–1994 mean and extreme locations (Lee, 1997).

this resolution, the core of the DWBC is not obvious everywhere, as the topography is smooth and the Gulf Stream has a strong barotropic component. At 25°N (Fig. 13), a near-bottom velocity maximum can be found in 2400 m with 2 cm/s southward flow, which, however, is displaced offshore from the core of the Gulf Stream. Comparison with DYNAMO results at 1/3° resolution (Willebrand et al., 2000) indicate that steeper slopes are necessary to obtain a realistic representation of the interplay between the Gulf Stream and the DWBC in this region.

All in all, many aspects of the Gulf Stream system are represented quite well in this non-eddy resolving configuration of ROMS (see also the time mean sea surface height, discussed below). Some features (notably the Gulf Stream separation pattern) are distinctly different from those found in prior simulations at comparable resolution, highlighting the complex influence of numerical and algorithmic choices on the large-scale dynamical processes.

#### 4.5. Mediterranean water tongue and Eastern basin circulation

The Mediterranean Water is injected into the Atlantic at its eastern boundary at about 35°N, forming a tongue of warm and salty anomaly on the 1000–1200 m depth horizon.

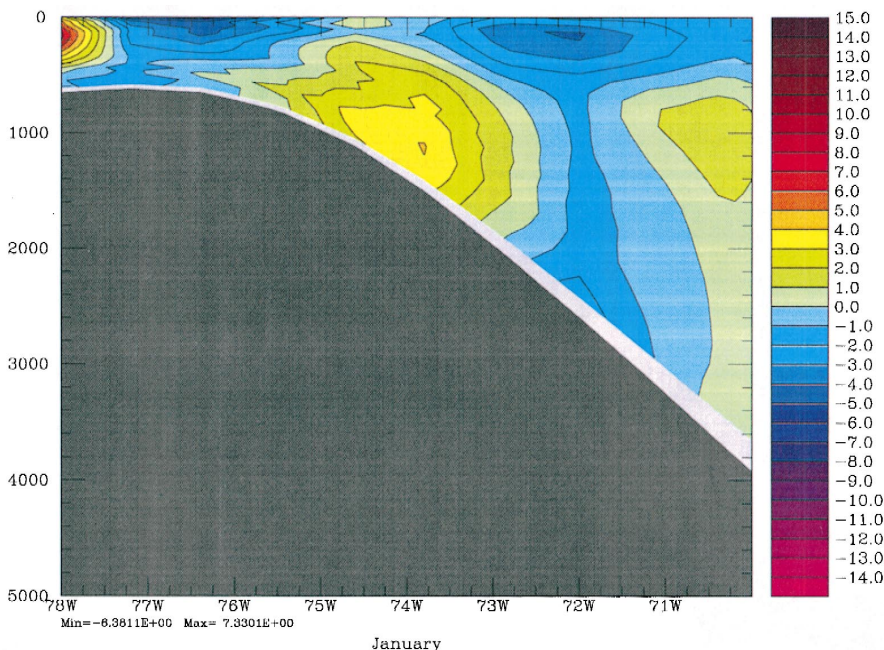


Fig. 13. Annual mean velocity (cm/s) cross-section along 25°N from E1.

This anomaly spreads a few hundred km westward and is advected northward with the poleward undercurrent along the European continental slopes. Present in the initial Levitus data, this tongue disappears within a decade, unless specific measures are taken to renew this water mass. A standard method is to use restoring to climatology (usually in the Gulf of Cadiz), but this has proven to be too inefficient in many models of the North Atlantic circulation (e.g., CME), unless the area of restoring is enlarged (to 5 by 5°). Gerdes et al. (1999) have recently shown for coarse resolution models that an inflow condition with about 3 Sv of highly anomalous water is probably the best way to parameterize the interaction of the Atlantic with the Mediterranean Sea across the Straits of Gibraltar.

Since restoring was used by consensus in the DAMEE experiments reported here, we cannot expect too much in this respect. Not surprisingly, only remnants of the Mediterranean Water tongue in 1200 m depth are visible after 10 years of integration (Fig. 14). Horizontal currents at this level of typically 8–10 cm/s are spatially non-uniform, but individual zonal flow bands can be identified (e.g. at 35°N and 38.5°N), which transport filaments of the Mediterranean Water offshore into the Labrador Sea Water. There is also a general tendency for a poleward undercurrent along the continental slope, as found in higher-resolution models (e.g., DG97). The majority of the high temperature, high salinity water is however gone, as seen in a comparison of Levitus and model TS diagrams (Fig. 15). Without a continuous source of water with salinities exceeding 36.5

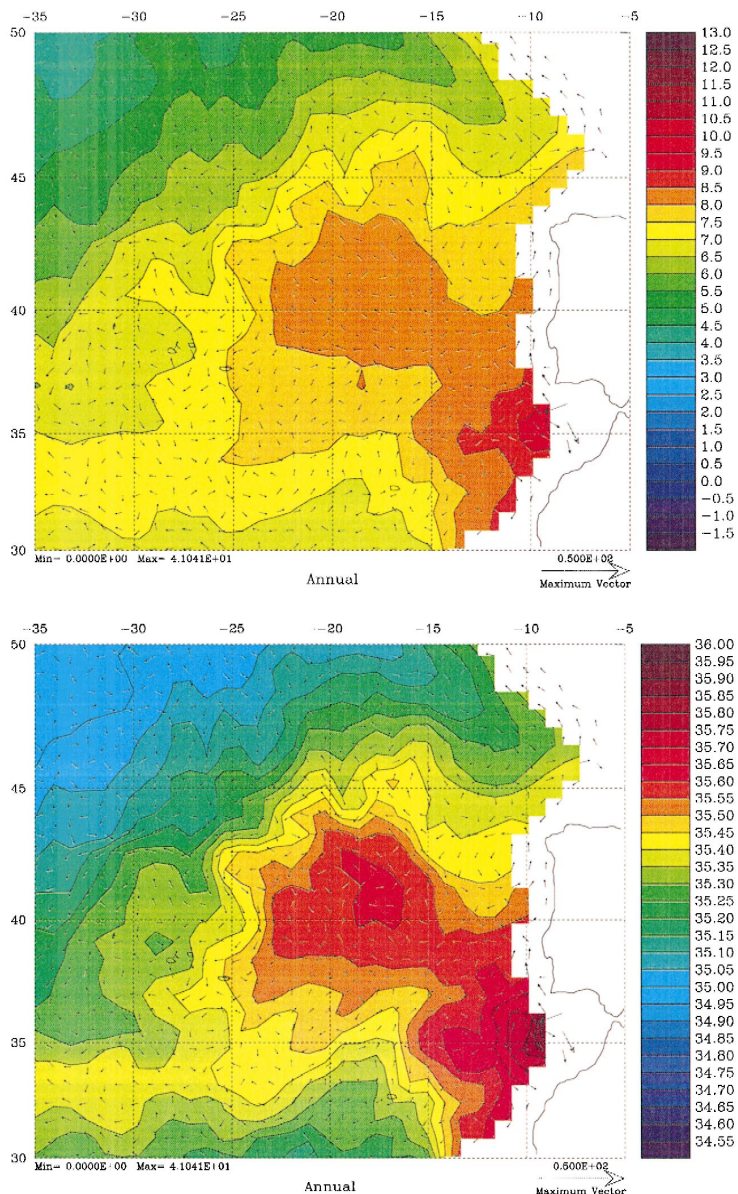


Fig. 14. The Eastern Basin at 1200 m depth from E1: (a) temperature ( $^{\circ}$ C) and horizontal velocity (cm/s), (b) salinity (PSU) and horizontal velocity (cm/s).

PSU, temperatures of more than  $11.8^{\circ}$ C and densities around  $\sigma_T = 27.9$ , a significant freshening takes place during the model integration. A similar evolution was noted in the CME experiments (Klinck, 1995). The apparently better representation of the Mediter-

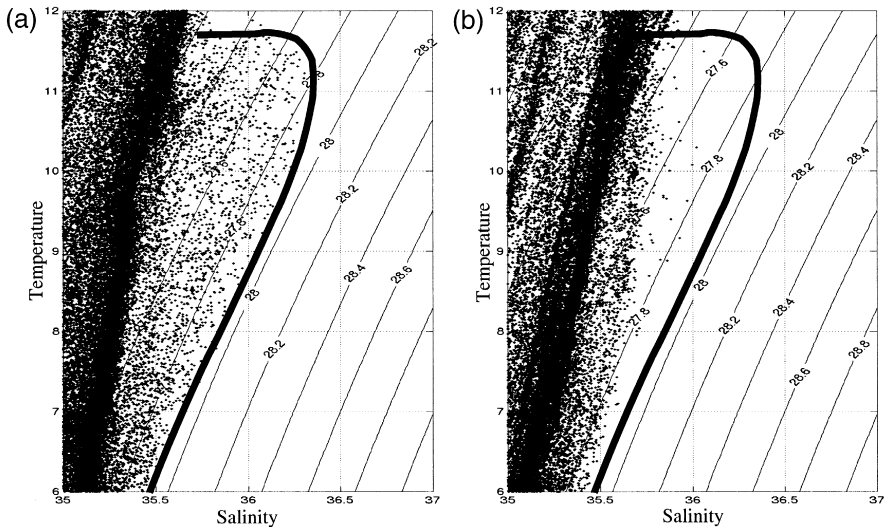


Fig. 15. Annual mean temperature–salinity diagrams from E1 showing the loss of Mediterranean water: (a) Levitus, (b) E1.

ranean water tongue in the isopycnic model presented by PCM00 may be due to a different efficiency of the restoring mechanism in isopycnic models, which acts on salinity and layer thickness rather than salinity and temperature (Killworth, 2000).

The Azores Current is a feature of the eastern North Atlantic that is difficult to capture in numerical circulation models. Its origin is thought to be the area south of Newfoundland, where it branches from the North Atlantic Current. In the eastern basin, observations show the Azores Current as a meandering zonal front with typical time–mean surface velocities of about  $20 \text{ cm s}^{-1}$ , at about  $35^\circ\text{N}$ . The Azores front is intimately linked to the subduction processes in the Northeastern Atlantic. It is unclear whether it is generated by the thermohaline forcing in this area or whether it is a wind-driven feature that happens to define the northward boundary of the subtropical mode water.

In the central ROMS case (Fig. 16), a broad, generally eastward flow can be identified between  $35^\circ\text{N}$  and  $40^\circ\text{N}$ , which turns southward outside the Gulf of Cadiz. This is very similar to the Sverdrup regime in the coarse ( $1^\circ$ ) resolution isopycnic simulation reported in PCM00. At higher resolution, the vertical coordinate seems to have a major effect; realizations with isopycnic models often reproduce this feature (e.g., DG97; PCM00), while it is less pronounced in simulations with sigma and geopotential coordinate models. The observed variability associated with the Azores Current is attributable to baroclinic instability. This eddy generation mechanism would require a potential vorticity extremum between  $30^\circ\text{N}$  and  $35^\circ\text{N}$  in eastern North Atlantic (Beckmann et al., 1994a). While present in the initial conditions, the model loses this potential vorticity maximum (see Fig. 10) and underestimates the variability along the front.

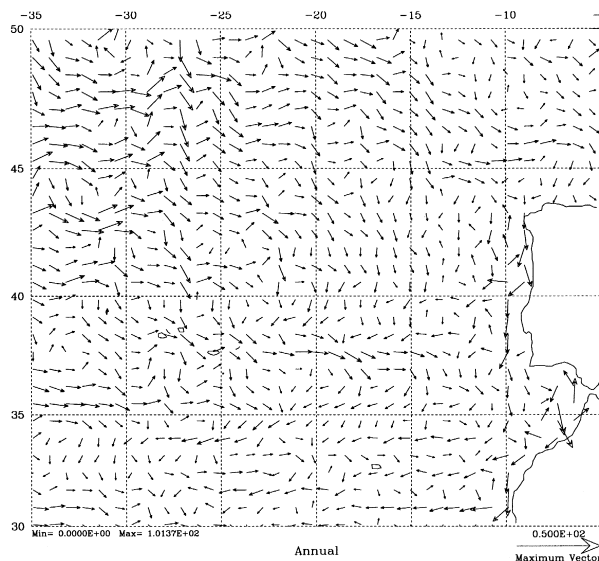


Fig. 16. Annual mean surface velocity (cm/s) in the eastern basin for E1.

#### 4.6. Mean and eddy sea surface height and sea surface temperature

At the rather coarse horizontal resolution employed in the central experiment, adequate representation of the mean and time-varying properties of SSH and SST may be problematic, particularly in regions of strong frontal dynamics and instabilities. Fig. 17, for example, shows the time-mean SSH and SSH variability obtained from the central ROMS experiment. In the time mean, a strong surface front in sea surface height does leave the western boundary at approximately the latitude of Cape Hatteras, as expected. The resulting SSH front proceeds into the basin towards the northeast, maintaining a well-defined integrity for about  $10^\circ$  of latitude before disappearing. At separation, the maximum SSH difference across the model Gulf Stream is close to 80 cm, about  $3/4$  of the value obtained from altimetric measurements and models of higher horizontal resolution (e.g., DG97, Fig. 4.17). While quite good for a model of this resolution, these properties clearly emphasize that the inertial character of the Gulf Stream is under-represented here, even with the weakly dissipative numerics employed in ROMS.

At a nominal resolution of  $3/4^\circ$ , internally generated variability should be modest, with most of the temporal fluctuations being directly forced by the seasonal atmospheric forcing. Nonetheless, measurable mesoscale variability in sea surface height does arise in three expected locations (Fig. 17b): the Gulf Stream system between  $80^\circ\text{W}$  and  $50^\circ\text{W}$ ; the Gulf of Mexico; and the western equatorial Atlantic along the coast of South America, where transient eddies are known to form and to propagate northwestwards. SSH variability is most intense in the first two of these regions, reaching mean-square values of approximately  $0.2 \text{ m}^2$ , or about 40 cm RMS. These extremal values in

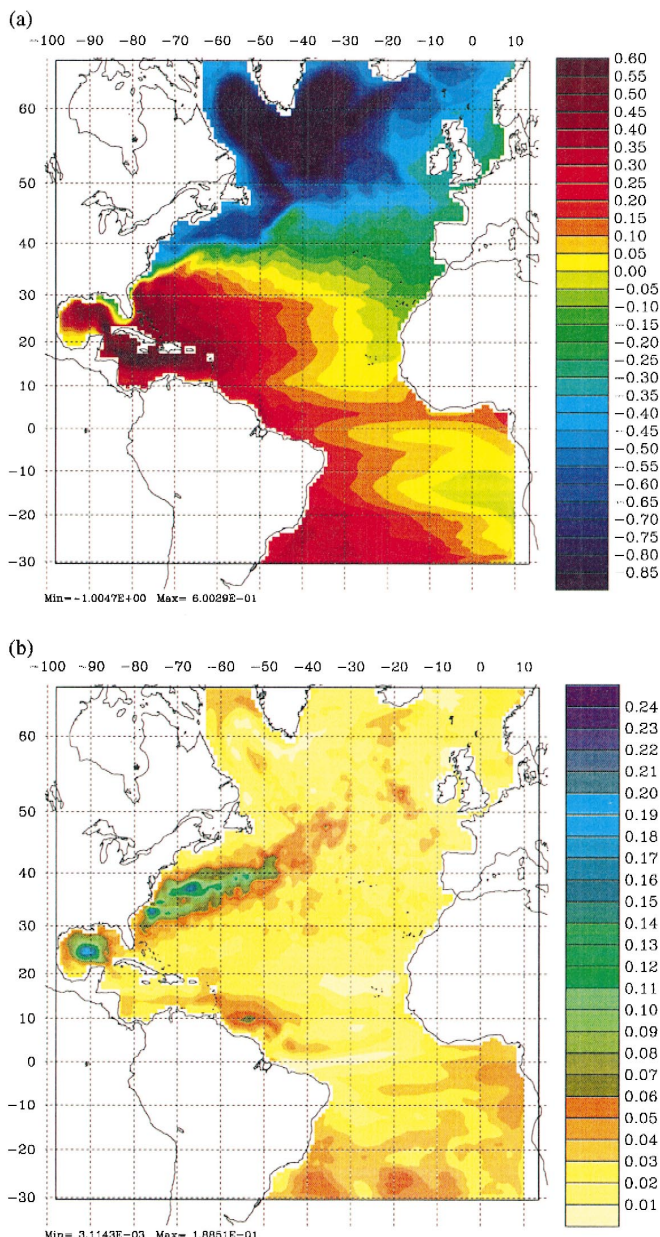


Fig. 17. Mean annual SSH (m) and SSH variability ( $\text{m}^2$ ) from E1.

variability are weaker by about 20% than those reported in the  $1/3^\circ$  DYNAMO simulations (DG97, Fig. 8.6), nor are they as spatially extensive as observed in reality.

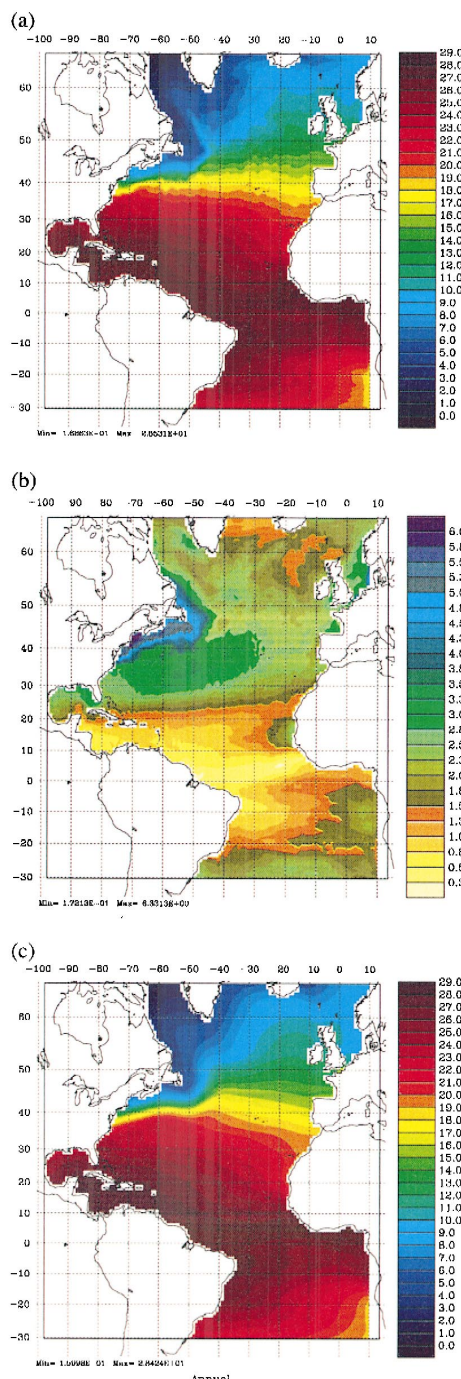


Fig. 18. Sea surface temperature (C): (a) E1 model mean, (b) E1 model variability, (c) Levitus and Boyer (1994).

The time-mean sea surface temperature and its variance are shown in Fig. 18. The mean temperature field at the surface does not depart appreciably from Levitus climatology, perhaps not a surprise given the surface heat flux correction term used in the upper boundary condition. Variability in SST is broadly distributed and enhanced to the north, indicative of seasonal heating/cooling influences. Little enhanced SST variability is noted in the neighborhood of the separated Gulf Stream or in the Gulf of Mexico, in agreement with the hypothesis that the local enhancement in SSH variability in these regions is a result of barotropic processes.

## 5. Sensitivity to model parameters

The seven additional experiments summarized in Table 1 were conducted to examine the impact of several configuration issues, including the choice of vertical coordinate parameters (E2), vertical resolution (E3), the surface salinity boundary condition (E4), domain size (also, location of the fictitious “open” boundaries relative to the area of interest; E5), horizontal resolution (E6), and advection algorithm (E7, E8). Although each of these changes produced some noticeable differences in solution behavior, only two (E4 and E6) could be said to generally improve upon the behavior of the central experiment. Three other experiments (E3, E7, E8) produced behavior largely similar to the central case, but with some sensitivities we describe below.

The two remaining experiments — the pure sigma case (E2), and the small domain simulation (E5) — both showed unilateral degradation of results. Neither of these findings is (to us) particularly surprising. With  $\theta = 0$ , and a uniform distribution of resolution in the resulting pure sigma coordinate, the upper water column is quite poorly represented (recall Fig. 2). As a consequence, surface forcing and associated water mass formation processes are hopelessly under-resolved. For example, Fig. 19 shows the depth of the simulated late winter planetary boundary layer for the central experiment and for E2. Note the unrealistic resemblance of the PBL thickness in E2 to the underlying topography. Over much of the basin, the thickness of the planetary boundary layer is over-estimated, leading to unrealistically deep vertical mixing of surface-supplied heat and momentum.

Under-resolution of surface forcing and associated dynamics results in several noticeable differences between experiments E2 and E1. Perhaps most interestingly, the intensity of the integrated circulation — e.g., kinetic energy (Fig. 4) and Florida Strait transport (Fig. 11) — are greatly enhanced, the latter well above observational estimates (This nicely underscores the point that the most energetic simulation is not always the best simulation). Also, the drift in global mean temperature is greatly accentuated with poor surface resolution (Fig. 5a). Given the flux-correction surface boundary condition being used for temperature, the enhanced global temperature drift is clearly a consequence of the overly deep mixing of heat by the under-resolved surface mixed layer processes. It is less clear why the kinetic energy and depth-integrated circulation should be similarly enhanced, though erroneously rapid vertical mixing of momentum might act to “shield” energy in the barotropic and gravest baroclinic modes.

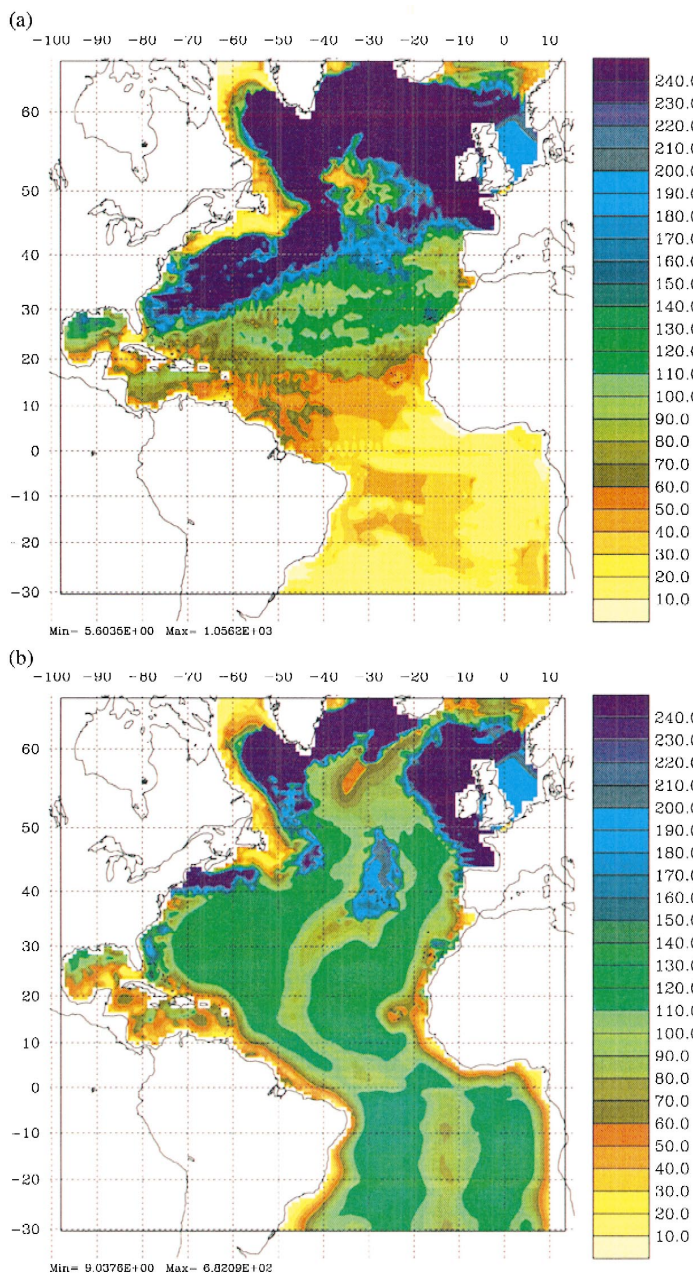


Fig. 19. Mean monthly planetary boundary layer thickness (m) for March: (a) E1, (b) E2.

The ROMS results obtained in the small domain are discussed in detail elsewhere in this volume. Given the generally negative experience with simple nudging boundary conditions — e.g., as reported above for the T/S nudging in the Gulf of Cadiz — we

are not surprised to find the results in our small domain experiment to be generally inferior to those obtained in the larger domain. In terms of its integrated properties, for instance, E5 had lower levels of kinetic energy (cf., Fig. 4) than any of the other  $3/4^{\circ}$  experiments, as well as an anomalously weak meridional heat transport (Fig. 9). In contrast to the behavior of the large-domain experiments, the Gulf Stream overshoots Cape Hatteras, hugging the coastal boundary until it finally detaches at about  $40^{\circ}\text{N}$ . Before heading eastwards, however, the detached current returns to the southwest, forming a deep, quasi-permanent meander, so that it eventually enters the deep ocean at approximately the correct latitude. Like E1, the Gulf Stream in the small domain deviates to the south at about  $62^{\circ}\text{W}$ .

A remaining mystery is why other models such as MICOM (PCM00) find so little difference between results obtained in large and small domains (We note in particular that the placement of the northern boundary in E5 cuts directly through the sub-polar gyre. It is not clear how this missing “information” can be supplied to the model via T/S nudging alone.). This is perhaps attributable to inherent differences in how isopycnic and non-isopycnic models interpret T/S nudging; see Killworth (2000). At least one other of the DAMEE models combined specified inflow along the northern open boundary with T/S nudging. It seems clear to us that this ought to work in principle. Simple variants on the T/S nudging boundary conditions which added some nudging of the free sea surface showed some improvement in our experience.

Improvements over the results of the central case were found to be primarily associated with two factors: replacement of the surface (E-P) salinity boundary condition with a relaxation to observed (Levitus) salinity, and enhancement of horizontal resolution. In terms of bulk water mass properties, the greatest degree of improvement is obtained from the former of these two factors (Similar dependencies were found in other of the DAMEE models — e.g., MICOM — and weak relaxation to surface salinity values was also used in DYNAMO). With the addition of surface relaxation to Levitus salinity, long-term drifts in the global inventory of salinity are greatly reduced, though they are still positive (Fig. 5b). Interestingly, experiments E4 and E6 also show an improved (decreased) drift in bulk temperatures (Fig. 5a), and a slowing (in E6) of the rate of temperature drift in the latter years of the experiment.

(We note parenthetically an interesting artifact of the choice of horizontal grid and the smoothing of topography necessitated by it. Fig. 5a,b shows that the initial value of volume-averaged temperature and salinity is greatly different for the grid used in experiments [E1,2,3,4,7,8] and that used in E6, the latter being a simple subdivision by two of the former, along with a redefinition of topography. The finer grid and steeper topography that goes with it result in much less “filling in” of the ocean margins. As a consequence, less deeper (and colder) water is excluded by this filling-in process. Initial values of volume-averaged temperatures are particularly affected — by  $0.2^{\circ}\text{C}$  — by these effects.)

In both E4 and E6, the resulting area-averaged vertical profiles of salinity are now in much closer agreement with Levitus climatology (Fig. 6). Transects along  $55^{\circ}\text{W}$  and  $30^{\circ}\text{W}$  (Fig. 20) show only weak, distributed anomalies in salt, except for a subsurface positive salinity anomaly to the north of the Gulf Stream along  $55^{\circ}\text{W}$ . Apparently, the fresh slope waters expected at this latitude (produced in reality by a combination of

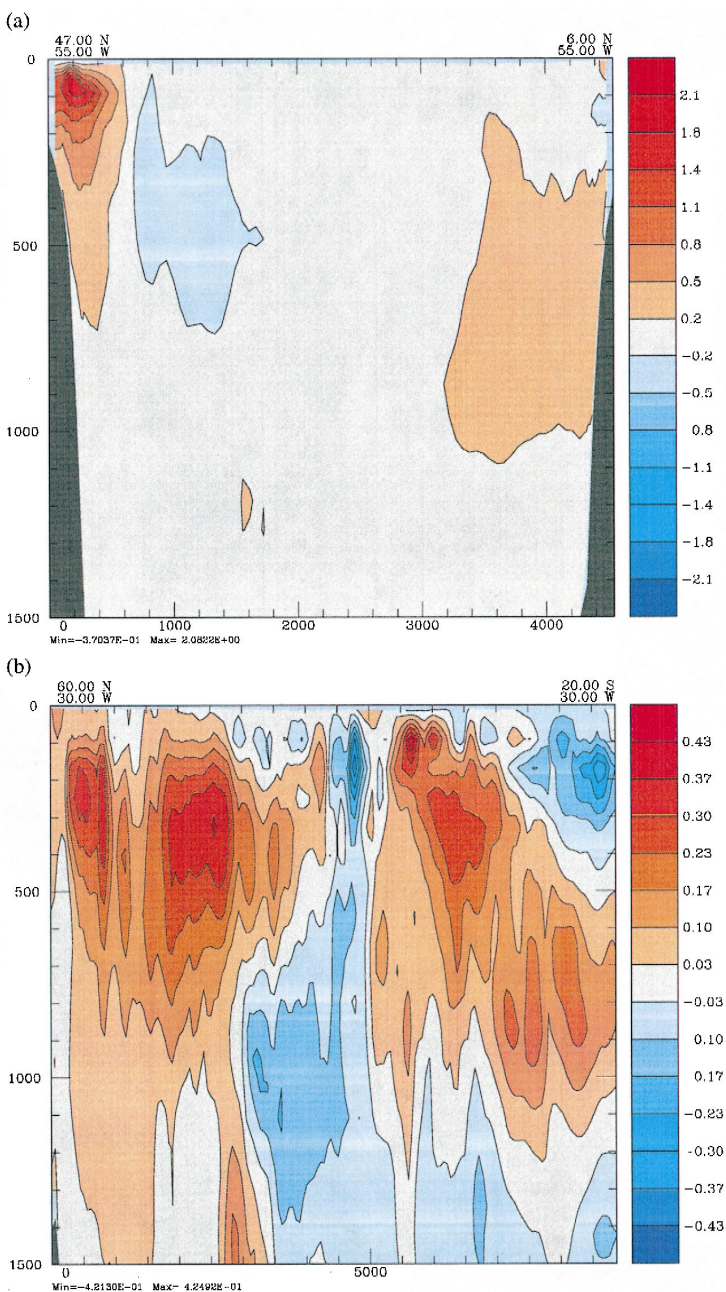


Fig. 20. Salinity anomaly from Levitus (PSU) for years 8–10 from E6, (a) 55°W, (b) 30°W.

freshwater runoff and advection from the north) are not being correctly reproduced by the model.

In the meridional distribution of late winter (March) potential vorticity (Fig. 21), we note several differences relative to the coarse resolution case (E1; see Fig. 10): the main thermocline maximum extends farther north and is connected to the North Atlantic Current signature, which is located deeper than in E1. Both features improve the agreement with observations. Still, at  $3/8^\circ$  grid spacing, we do not see a pronounced maximum in the Azores Current region, and conclude that this requires even more resolution (Beckmann et al., 1994b; Smith et al., 2000). The meridional overturning streamfunction is also influenced by the enhanced horizontal resolution (Fig. 22). Although somewhat lower in overall amplitude than in the central experiment, the overturning streamfunction is now centered deeper in the water column (now near  $z \approx -1000$  m), and extends farther north. Both changes are in the direction of inferred patterns of meridional transport. Despite these structural changes in the overturning streamfunction, the net meridional heat transport is not significantly altered by the increased horizontal resolution (Fig. 9).

It is expected that increased horizontal resolution will be accompanied by enhanced levels of internal variability. For comparison with E1, Fig. 23 shows sea surface height variability from the high-resolution experiment and comparable estimates from TOPEX. Significant SSH variability is now found also in the Gulf of Mexico and the North Brazil Current area, a signature of better resolved North Brazil Current eddies (see also Barnier et al., 2000). Strong variability in the region of the Gulf Stream also extends

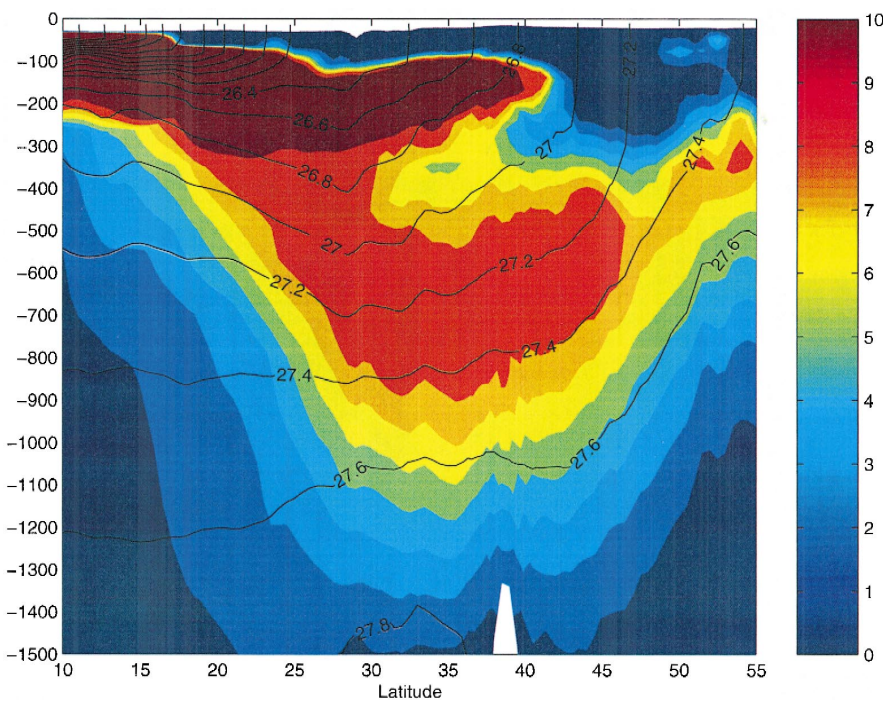


Fig. 21. Potential vorticity ( $10^{-11} \text{ m}^{-1} \text{ s}^{-1}$ ) for March in E6 along  $30^\circ\text{W}$ .

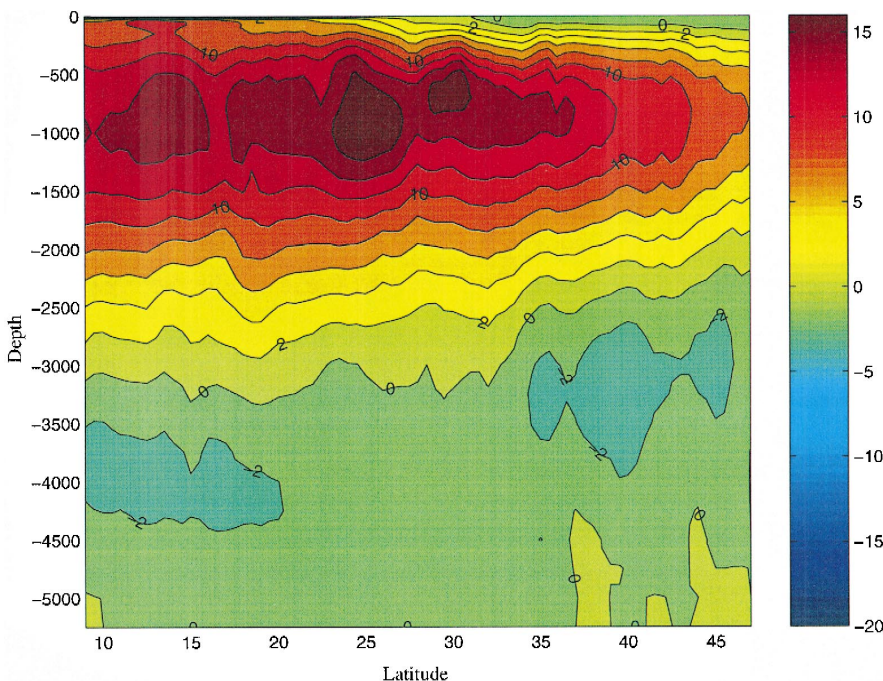


Fig. 22. Mean annual meridional overturning streamfunction for E6 (Sv).

well east (to  $30^{\circ}\text{W}$ ), indicative of stronger eastward penetration of the Gulf Stream front. From the Northwest Corner ( $40^{\circ}\text{W}$ ,  $50^{\circ}\text{N}$ ) a branch of increased variability extends into the Labrador Sea, following the continental slope as found in other sigma-coordinate model realizations (e.g., DG97). Though generally lower in amplitude by perhaps a factor of about two than estimates obtained from TOPEX, the level and patterns of variability of the  $3/8^{\circ}$  resolution experiment (E6) are (at least) of comparable realism to results obtained from other OGCMs of equivalent ( $\approx 1/3^{\circ}$ ) resolution.

Lastly, we note the (generally lesser) impacts produced by heightened vertical resolution and the use of more traditional (centered) advection algorithms (experiments E3, E7, E8; Table 1) (Recall that the use of centered advection required the adoption of finite values for biharmonic viscosity and diffusivity, so that more than just advection was being modified). In terms of bulk energetics, the differences observed in these last three experiments were not dramatic, although the high-order centered advection run produced more energetic horizontal (e.g., kinetic energy; Fig. 4) and vertical (meridional heat transport, Fig. 9) circulations than in E1 by about 15%.

Differences of similar magnitude are seen in the bulk tracer fields (Fig. 5) in which the temperature drifts are seen to improve in E3/E7/E8, and the salinity drifts to reverse in sign but to remain of comparable magnitude. These effects are difficult to explain in any simple, single way. The explicit biharmonic smoothing added to the centered advection runs can be expected to operate differently on tracers than the

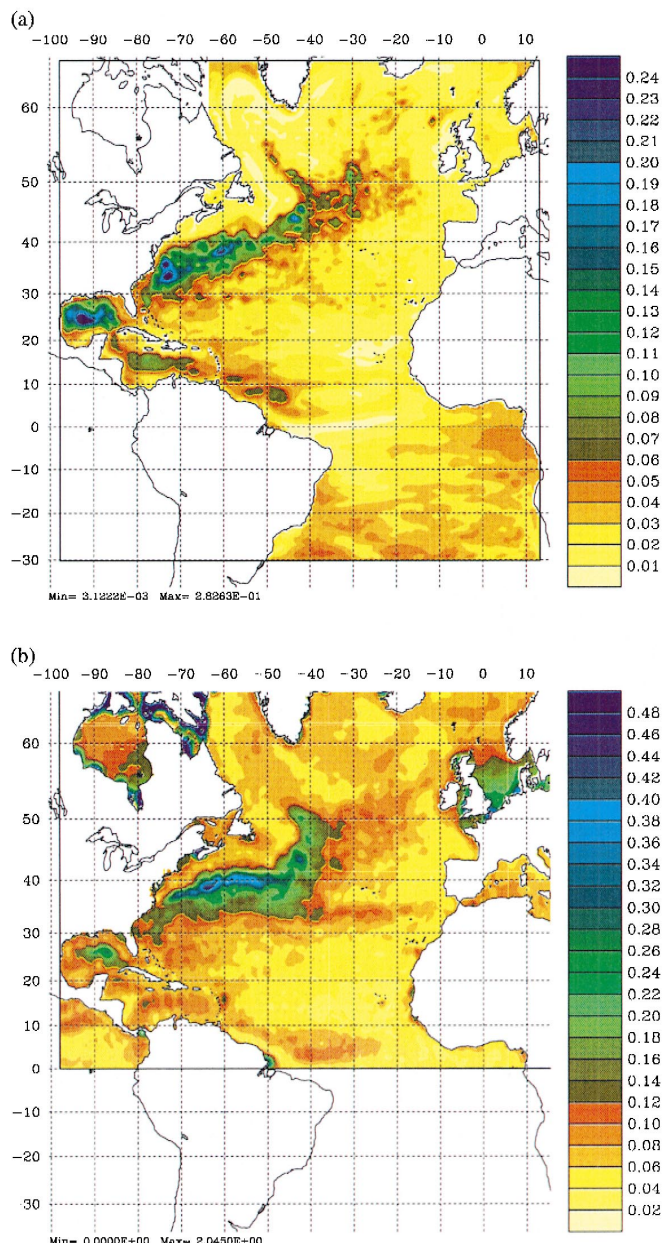


Fig. 23. Sea surface height variability ( $\text{m}^2$ ): (a) E6 and (b) Topex (from Gregg Jacobs, NRL).

scale-selective smoothing associated with the TOUS scheme. However, experiment E3 utilized the same advection/diffusion mechanisms as did E1, though added vertical resolution may be assumed to have some impact on vertical mixing via the KPP scheme.

If there is a single explanation for the differences in tracer inventories between E1 (positive drifts in T and S) and E3/E7/E8 (reduced T drift, negative drift in S) it may therefore be that the three latter experiments experienced similar patterns of change in vertical (diapycnal) mixing, though perhaps for very different reasons.

## 6. Summary and discussion

A systematic survey of results from the ROMS terrain-following NAB model has been described. The primary conclusion we draw is that ROMS is able to reproduce known measures of both the wind-driven and thermohaline circulation, and to do so within error bounds comparable with prior model simulations (e.g., CME and DY-NAMO). Quantitative comparison with DAMEE/MICOM (PCM00) also confirm that our terrain-following solutions are of similar overall quality when viewed against known measures of merit including meridional overturning and heat flux, Florida Straits and Gulf Stream transport, seasonal cycling of temperature and salinity, and upper ocean currents and tracer fields in the eastern North Atlantic Basin. Departure from prior experience is most significant in the ability of the present model to produce a Gulf Stream path close to that observed, at least out to about 62°W.

Parametric and algorithmic sensitivities have been shown to exist which span an enormous range of model behaviors. If any clear conclusions may be drawn in this regard, the first would seem to be that further simultaneous enhancements in horizontal resolution and topographic realism are essential to do a better job on the structure and strength of the DWBC. Second, the choice of domain size and “open” boundary conditions must be made with care; results obtained within the smaller DAMEE-consensus domain were universally poor in comparison to those obtained in the larger basin [though not so in MICOM/DAMEE (PCM00)]. Lastly, great sensitivity of water mass formation and long-term bulk tracer inventories is displayed to alternate forms of surface salinity boundary conditions. Unfortunately, the most “realistic” result — i.e., the least drift from Levitus and Boyer (1994) and Levitus et al. (1994) — is obtained with the least physically satisfying surface boundary condition, and further exploration of physically plausible surface boundary conditions leading to lower overall tracer drift is necessary.

Several technical features of ROMS have proven consequential to the degree of skill shown in these simulations. The first of these is the nonlinear stretched vertical coordinate whose simultaneous ability to be terrain-following near the bottom and (nearly) surface-following in the upper water column has been shown to produce sensible surface boundary layer response and water mass formation at modest vertical resolution (See also Malanotte-Rizzoli et al., 2000). An alternative to the stretched vertical coordinate is the use of a standard sigma coordinate ( $\theta = 0$ ) but with unequal grid spacing favoring the ocean surface. Unfortunately, the latter approach is only first-order accurate in the vertical, with potentially troublesome truncation error properties (e.g., Haidvogel and Beckmann, 1999).

A second source of technical improvement in these simulations are the revised procedures for split-explicit time-stepping, which have led to a simultaneous increase in

both accuracy and efficiency. Taken together with the improved parallel performance of the new ROMS, multi-decadal simulations at basin-to-global scales are now feasible on rather modest numbers of processors. A high-performance version of ROMS for use in distributed-memory environments is nearing completion, and should extend this computing capability to (e.g.) Beowulf-class clusters of PC's and workstations.

Lastly, replacement of traditional centered algorithms for advection of tracers and momentum with approximately monotone, scale-selective advection schemes offers the prospect of increasingly accurate representations of dynamical processes on fine spatial scales (frontal evolution, mesoscale eddies, etc.). As seen herein, even at non-eddy-resolving resolution, differences in behavior are closely allied with choice of advection algorithm (and the related requirements for explicit subgrid-scale smoothing operators). Unfortunately, the ultimate causes for these sensitivities are often difficult to sort out in a fully realistic setting. Further development and intercomparison of weakly dissipative approaches to tracer advection — whether by higher-order, centered forms or via upstream treatments — and their assessment on standardized test problems having quantifiable standards of merit are needed.

Though there is much to be gained by further exploration of the ROMS model in prognostic mode, imperfections in forcing data, excluded physics and finite space/time resolution all conspire to render any numerical solution approximate and uncertain. The inevitable errors that result occur on both fine space/time scales (e.g., the instantaneous location and strength of eddies, fronts, convection, etc.) and on the scales of the global equilibrium climate (e.g., model tracer drift). Many important modeling objectives, real-time operational prediction and long-term climate modeling among them, are therefore not easily achievable via prognostic modeling alone. Systematic means of model/data assimilation need to be assessed towards the dual goals of routine and skillful basin-wide oceanic prediction, and accurate global climate modeling. Such assessments are presently underway using ROMS and the reduced-state Kalman filter.

## Acknowledgements

Development of the ROMS model and its application within DAMEE have been supported by the Office of Naval Research under grants number N00014-93-1-0197 to Rutgers University and N00014-95-1-0226 to MIT. Additional support for ROMS development has been provided by NSF/EPA to UCLA. The helpful comments of both anonymous reviewers significantly improved the presentation and content of this work. The final versions of this manuscript were prepared by the first author while on leave at the University of California, Berkeley. The support of the Miller Institute for Basic Research in Science during this period is gratefully acknowledged.

## References

- Arakawa, A., Lamb, V.R., 1977. In: *Methods of Computational Physics* 17 Academic Press, pp. 174–265.
- Barnier, B., Siefridt, L., Marchesiello, P., 1995. Thermal forcing of a global ocean circulation model using a three-year climatology of ECMWF analyses. *J. Mar. Sys.* 6, 363–380.

- Barnier, B., Marchesiello, P., de Miranda, A.P., Molines, J.-M., Coulibaly, M., 1998. A sigma-coordinate primitive equation model for studying the circulation in the South Atlantic. Part I: Model configuration with error estimates. Deep Sea Res. 45, 543–572.
- Barnier, B., Reynaud, T., Beckmann, A., Böning, C., Molines, J.M., Barnard, S., Jia, Y., 2000. On the seasonal variability and eddies in the North Brazil Current: insights from model intercomparison experiments. Prog. Oceanogr., submitted.
- Beckmann, A., Haidvogel, D.B., 1993. Numerical simulation of flow around a tall isolated seamount. Part I: Problem formulation and model accuracy. J. Phys. Oceanogr. 23, 1736–1753.
- Beckmann, A., Böning, C.W., Brügge, B., Stammer, D., 1994a. Eddy variability in the central North Atlantic Ocean: Results from surface drifters, satellite altimetry and numerical modeling. J. Geophys. Res. 99, 20381–20391.
- Beckmann, A., Böning, C.W., Köberle, C., Willebrand, J., 1994b. Effects of increased horizontal resolution in a simulation of the North Atlantic Ocean. J. Phys. Oceanogr. 24, 326–344.
- Bleck, R., Rooth, C., Hu, D., Smith, L., 1992. Salinity-driven thermocline transients in a wind- and thermohaline-forced isopycnic coordinate model of the North Atlantic. J. Phys. Oceanogr. 22, 1486–1505.
- Böning, C.W., Bryan, F., 1996. Large-scale transport processes in high-resolution circulation models. In: Krauss, W. (Ed.), The Warmwatersphere of the North Atlantic Ocean. Gebr. Borntraeger, Berlin, Stuttgart, pp. 91–128.
- Bryan, K., 1969. A numerical method for the study of the circulation of the world ocean. J. Comput. Phys. 4, 347–376.
- Bryan, F.O., Holland, W.R., 1989. A higher-resolution simulation of the wind and thermohaline-driven circulation in the North Atlantic ocean. In: Muller, P., Anderson, D. (Eds.), Parameterization of Small-Scale Processes. Proceedings Aha Huliko's Hawaiian Winter Workshop.
- Chassignet, E.P., Smith, L.T., Bleck, R., Bryan, F.O., 1996. A model comparison: Numerical simulations of the North and Equatorial Atlantic Oceanic Circulation in Depth and isopycnic coordinates. J. Phys. Oceanogr. 26, 1849–1867.
- Chu, P.C., Fan, C., 1997. Sixth-order difference scheme for sigma coordinate ocean models. J. Phys. Oceanogr. 27, 2064–2071.
- Cox, M.D., 1984. A primitive equation three-dimensional model of the ocean. Tech. Rep. 1. GFDL Ocean Group, Princeton University, 250 pp.
- DaSilva, A.M., Young, C.C., Levitus, S., 1994. Atlas of Surface Marine Data. .
- Dengg, J., Beckmann, A., Gerdes, R., 1996. The Gulf Stream separation problem. In: Krauss, W. (Ed.), The Warmwatersphere of the North Atlantic Ocean. Gebr. Borntraeger, Berlin, Stuttgart, pp. 253–290.
- DYNAMO group [Barnard, S., Barnier, B., Beckmann, A., Böning, C.W., Coulibaly, M., DeCuevas, D'A., Dengg, J., Dieterich, Ch., Ernst, U., Herrmann, P., Jia, Y., Killworth, P.D., Kröger, J., Lee, M.-M., LeProvost, Ch., Molines, J.-M., New, A.L., Oschlies, A., Reynaud, T., West, L.J., Willebrand, J.], 1997. DYNAMO - Dynamics of North Atlantic Models: simulation and assimilation with higher-resolution models. Ber. Inst. f. Meereskunde Kiel 294, 333 pp.
- Gary, J.M., 1973. Estimation of truncation errors in transformed coordinate, primitive equation atmospheric models. J. Atmos. Sci. 30, 223–233.
- Gerdes, R., Köberle, C., Beckmann, A., Herrmann, P., Willebrand, J., 1999. Mechanisms for spreading of Mediterranean Water in coarse resolution numerical models. J. Phys. Oceanogr. 29, 1682–1700.
- Haidvogel, D.B., Beckmann, A., 1998. Numerical modeling of the coastal ocean. In: Brink, K.H., Robinson, A.R. (Eds.), The Sea 10 pp. 457–482.
- Haidvogel, D.B., Beckmann, A., 1999. Numerical Ocean Circulation Modelling. Imperial College Press, London, 318 pp.
- Haidvogel, D.B., Wilkin, J.L., Young, R.E., 1991. A semi-spectral primitive equation ocean circulation model using vertical sigma and orthogonal curvilinear horizontal coordinates. J. Comput. Phys. 94, 151–185.
- Haidvogel, D.B., McWilliams, J.C., Gent, P.R., 1992. Boundary current separation in a quasigeostrophic, eddy-resolving ocean circulation model. J. Phys. Oceanogr. 22, 882–902.
- Haney, R.L., 1991. On the pressure gradient force over steep topography in sigma coordinate ocean models. J. Phys. Oceanogr. 21, 610–619.
- Hedström, K.S., 1994. User's Manual for a Semi-spectral Primitive Equation Ocean Circulation Model. Version 3.9. Institute of Marine and Coastal Sciences, Rutgers University, 131 pp.

- Hedström, K.S., 1997. User's Manual for an s-coordinate Primitive Equation Ocean Circulation Model (SCRUM: Version 3.0). Institute of Marine and Coastal Sciences, Rutgers University.
- Jackett, D.R., McDougall, T.J., 1995. Stabilization of hydrographic data. *J. Atmos. Oceanic Technol.* 12, 381–389.
- Killworth, P.D., 2000. Relaxation towards observations in level and isopycnic models. *J. Atmos. Oceanic Technol.*, submitted.
- Klinck, J.M., 1995. Thermohaline structure of an eddy-resolving North Atlantic model: the influence of boundary conditions. *J. Phys. Oceanogr.* 25, 1174–1195.
- Large, W.G., McWilliams, J.C., Doney, S.C., 1994. Oceanic vertical mixing: a review and a model with a nonlocal boundary layer parameterization. *Rev. Geophys.* 32, 363–403.
- Lee, H., 1997. A Gulf Stream Synthetic Geoid for the TOPEX Altimeter. M.S. Thesis, Rutgers University, New Brunswick, NJ, 36 pp.
- Levitus, S., Boyer, T.P., 1994. World ocean atlas 1994. Volume 4: Temperature. NOAA Atlas NESDIS 4, NOAA, Washington D.C.
- Levitus, S., Burgett, R., Boyer, T.P., 1994. World ocean atlas 1994. Volume 3: Salinity. NOAA Atlas NESDIS 3, NOAA, Washington D.C.
- MacDonald, A., 1995. Oceanic fluxes of mass, heat and freshwater: A global estimate and perspective. Ph.D. thesis, MIT-WHOI Joint Program.
- MacDonald, A., Wunsch, C., 1996. An estimate of global ocean circulation and heat fluxes. *Nature* 382, 436–439.
- Malanotte-Rizzoli, P., Hedstrom, K., Arango, H., Haidvogel, D.B., 2000. Water mass pathways between the subtropical and tropical ocean in a climatological simulation of the North Atlantic Ocean circulation. *Dyn. Atmos. Oceans* 32, 209–237.
- Marsh, R., Roberts, M.J., Wood, R.A., New, A.L., 1996. An intercomparison of a Bryan-Cox-Type Ocean model and an isopycnic ocean model. Part II. The subtropical gyre and meridional heat transport. *J. Phys. Oceanogr.* 26, 1528–1551.
- McCalpin, J.D., 1994. A comparison of second-order and fourth-order pressure gradient algorithms in a  $\sigma$ -coordinate ocean model. *Int. J. Numer. Methods Fluids* 18, 361–383.
- Mellor, G.L., Ezer, T., Oey, L.-Y., 1994. The pressure gradient conundrum of sigma coordinate ocean models. *J. Atmos. Oceanic Technol.* 11, 1126–1134.
- National Geophysical Data Center, 1988. Digital relief of the surface of the Earth. Data Announcement 88-MGG-02, NOAA, Boulder.
- Pacanowski, R.C., 1996. MOM2 Documentation, User's Guide and Reference Manual, GFDL Ocean Technical Report 3.2.
- Paiva, A.M., Hargrove, J.T., Chassignet, E.P., Bleck, R., 1999. Turbulent behavior of a fine mesh ( $1/12^\circ$ ) numerical simulation of the North Atlantic. *J. Mar. Sys.* 21, 307–320.
- Paiva, A.M., Chassignet, E.P., Mariano, A.J., 2000. Numerical simulation of the North Atlantic subtropical gyre: sensitivity to boundary conditions. *Dyn. Atmos. Oceans* 32.
- Phillips, N.A., 1957. A coordinate system having some special advantages for numerical forecasting. *J. Met.* 14, 184–185.
- Roberts, M.J., Marsh, R., New, A.L., Wood, R.A., 1996. An intercomparison of a Bryan-Cox-Type Ocean model and an isopycnic ocean model. Part I. The subpolar gyre and high-latitude processes. *J. Phys. Oceanogr.* 26, 1495–1527.
- Robinson, M., Bauer, R., Schroeder, R., 1979. Atlas of the North Atlantic — Indian Ocean Monthly Mean Temperatures and Mean Salinities of the Surface Layer. Dept. of the Navy, Washington D.C., USA.
- Shchepetkin, A.F., McWilliams, J.C., 1998. Quasi-monotonic advection schemes based on explicit locally adaptive dissipation. *Mon. Weather Rev.* 126, 1541–1580.
- Schott, F., Molinari, R.L., 1996. The western boundary circulation of the subtropical warmwatersphere. In: Krauss, W. (Ed.), *The Warmwatersphere of the North Atlantic Ocean*. Gebr. Borntraeger, Berlin, Stuttgart, pp. 229–252.
- Smith, R.D., Maltrud, M.E., Bryan, F.O., Hecht, M.W., 2000. Numerical simulation of the North Atlantic Ocean at  $1/10^\circ$ . *J. Phys. Oceanogr.*, submitted.

- Song, Y., Haidvogel, D.B., 1994. A semi-implicit ocean circulation model using a generalized topography-following coordinate. *J. Comput. Phys.* 115, 228–244.
- Willebrand, J., Barnier, B., Böning, C., Dieterich, Ch., Killworth, P., LeProvost, C., Jia, Y., Molines, J.-M., New, A.L., 2000. Circulation characteristics in three eddy-permitting models of the North Atlantic. *Prog. Oceanogr.*, submitted.